remote sensing

MDPI

Article

The Impacts of Air Quality on Vegetation Health in Dense Urban Environments: A Ground-Based Hyperspectral Imaging Approach

Farid Qamar [1,2,3,*], Mohit S. Sharma [4] and Gregory Dobler [2,3,4,5]

[1] Department of Civil and Environmental Engineering, University of Delaware, Newark, DE 19716, USA
[2] Biden School of Public Policy and Administration, University of Delaware, Newark, DE 19716, USA
[3] Data Science Institute, University of Delaware, Newark, DE 19716, USA
[4] Center for Urban Science and Progress, New York University, New York, NY 10003, USA
[5] Department of Physics and Astronomy, University of Delaware, Newark, DE 19716, USA
* Correspondence: qamar@udel.edu

Abstract: We examine the impact of changes in ozone (O_3), particulate matter ($PM_{2.5}$), temperature, and humidity on the health of vegetation in dense urban environments, using a very high-resolution, ground-based Visible and Near-Infrared (VNIR, 0.4–1.0 μm with a spectral resolution of 0.75 nm) hyperspectral camera deployed by the Urban Observatory (UO) in New York City. Images were captured at 15 min intervals from 08h00 to 18h00 for 30 days between 3 May and 6 June 2016 with each image containing a mix of dense built structures, sky, and vegetation. Vegetation pixels were identified using unsupervised *k*-means clustering of the pixel spectra and the time dependence of the reflection spectrum of a patch of vegetation at roughly 1 km from the sensor that was measured across the study period. To avoid illumination and atmospheric variability, we introduce a method that measures the ratio of vegetation pixel spectra to the spectrum of a nearby building surface at each time step relative to that ratio at a fixed time. This "Compound Ratio" exploits the (assumed) static nature of the building reflectance to isolate the variability of vegetation reflectance. Two approaches are used to quantify the health of vegetation at each time step: (*a*) a solar-induced fluorescence indicator (*SIFi*) calculated as the simple ratio of the amplitude of the Compound Ratio at 0.75 μm and 0.9 μm, and (*b*) Principal Component Analysis (PCA) decomposition designed to capture more global spectral features. The time dependence of these vegetation health indicators is compared to that of O_3, $PM_{2.5}$, temperature, and humidity values from a distributed and publicly available in situ air quality sensor network. Assuming a linear relationship between vegetation health indicators and air quality indicators, we find that changes in both SIF indicator values and PC amplitudes show a strong correlation (r^2 value of 40% and 47%, respectively) with changes in air quality, especially in comparison with nearby buildings used as controls (r^2 value of 1% and 4%, respectively, and with all molecular correlations consistent with zero to within 3σ uncertainty). Using the SIF indicator, O_3 and temperature exhibit a positive correlation with changes in photosynthetic rate in vegetation, while $PM_{2.5}$ and humidity exhibit a negative correlation. We estimate full covariant uncertainties on the coefficients using a Markov Chain Monte Carlo (MCMC) approach and demonstrate that these correlations remain statistically significant even when controlling for the effects of diurnal sun-sensor geometry and temperature variability. This work highlights the importance of quantifying the effects of various air quality parameters on vegetation health in urban environments in order to uncover the complexity, covariance, and interdependence of the numerous factors involved.

Keywords: remote sensing; urban science; solar-induced fluorescence; principal component analysis; ozone; particulate matter; temperature; humidity; MCMC

Citation: Qamar, F.; Sharma, M.S.; Dobler, G. The Impacts of Air Quality on Vegetation Health in Dense Urban Environments: A Ground-Based Hyperspectral Imaging Approach. *Remote Sens.* **2022**, *14*, 3854. https://doi.org/10.3390/rs14163854

Academic Editor: Austin Troy

Received: 15 June 2022
Accepted: 5 August 2022
Published: 9 August 2022

1. Introduction

Even though cities cover less than 5% of the US land surface [1] and 0.5% of global land cover [2], urban air quality has become a universal concern. As of 2018, the urban population has swelled to 55% of the world's population and is projected to reach up to 68% by the year 2050 [3]. This increased rate of urbanization is accompanied by an increased volume of motorized traffic, industrialization, energy use, and consequently an increase in air pollution [4–6]. Long-term exposure to air pollution has been shown to be associated with significant adverse health effects [7–10], and is ranked as one of the top five risk factors for mortality of the past two decades [11]. The effects of air quality are not only reflected in human health, but also in plants and vegetation. Plant injury and damage due to air pollution were discovered as early as the 1870s [12], and have been extensively studied throughout the past century [13–16].

Increased atmospheric particulate matter with diameter less than 2.5 μm ($PM_{2.5}$) has shown a significant negative correlation with biochemical parameters in plants, a reduction in stomata and chlorophyll content, as well as increased stress-induced enzyme activity [17–19]. These effects are reflected in plants' photosynthetic rates, which have been detected at rates 50% lower in industrial areas high in $PM_{2.5}$ relative to those in control areas [20]. Adverse effects on tree biomass and visible leaf injury have also been shown to be caused by surface ozone (O_3), which results in decreased chlorophyll content and, therefore, decreased photosynthesis [21–24]. These harmful effects have been discovered in agricultural crops [25,26] and forests [27–29].

However, it is important to note that studies assessing ozone damage to vegetation are traditionally conducted under controlled environmental conditions using plant chambers to expose plants to known O_3 concentrations [30,31]. The numerous variables that compose the environment in urban areas have complex correlations, covariances, and dependencies that can significantly change their expected impact on urban vegetation. For example, studies on the impact of ambient O_3 concentrations on urban vegetation suffer from the inability to separate the effects of O_3 from those of other urban pollutants and stressors using direct observations mainly due to the nature of ozone not accumulating in plant tissue or causing any unique signatures [32,33], as well as the need for O_3 concentrations to exceed 200–300 ppb for their effects to be measurable in vegetation [28]. Furthermore, strong correlations between O_3 concentrations and surface temperatures have been uncovered over multiple time-scales [34–36]. These correlations are made more complex with the existence of $PM_{2.5}$ and humidity levels, as well as the occurrence of the urban heat island effect, urban winds, and numerous other natural and anthropogenic factors [37,38].

Moreover, plant phenology, the seasonally recurring patterns of environment-mediated growth and development of plants, is heavily dependent on changes in temperature and moisture. Temperature is often regarded as the primary trigger of the timing of plant phenological events [39,40]. Leaf spring unfolding, blooming and flowering, and coloring and falling in autumn are processes mainly controlled by changes in temperature. Low temperatures activate plant stress response and induce endodormancy, and a certain accumulated amount of chilling breaks endodormancy and leads to ecodormancy, while the accumulation of warm temperatures accelerates plant cell growth [41]. Due to climate change and rising global temperatures, studies have reported significant advances in spring unfolding [42], a shift to earlier blooming [43], and a delay in autumn leaf coloring [44]. These effects are further exacerbated in cities due to the urban heat island effect [45]. Furthermore, studies have shown that moisture and humidity act as potential secondary triggers to various phenological events, including the timing of spring and autumn phenology [46,47], and flowering cycles [48]. Although detailed investigations are lacking, urbanization has a measurable impact on air humidity, precipitation, runoff, and groundwater retention, which has been found to influence plant phenology [49,50].

The traditional practice for obtaining data on vegetation health, phenological changes, and vegetation diversity is through physical sample collection and ground-based in situ observations [50,51]. These methods remain highly valuable as they provide first-hand

direct evidence of vegetation health, and record accurate species and site information. However, in situ observations tend to be uneven in distribution as they often require different observers and can vary in methodology and rigor. In the past two decades, Hyperspectral Imaging (HSI) has emerged as a non-invasive, near real-time tool for evaluating and monitoring the condition of vegetation [52–54]. Modern hyperspectral imaging acquires images in several hundred to thousands of spectral bands, thus allowing for a detailed spectral curve to be obtained for each spatial pixel in the image [55]. This increase in spectral resolution has been used in the studies of vegetation for the detection of disease symptoms and pests [56–58], as well as monitoring plant health, stress conditions, and nutrient deficiency [59–61]. Since air quality has a measurable effect on the morphological, physiological, and phenological properties of vegetation, these effects are reflected in the spectra of the vegetation, and therefore detectable using vegetation indices such as the Normalized Difference Vegetation Index (NDVI) [62] or the Photochemical Reflectance Index (PRI) [63] extracted from hyperspectral imaging. For example, in a 2019 study, [64] used aerial hyperspectral data (HyMap—126 spectral bands spanning 0.45–2.5 µm, and 5 m spatial resolution) to derive forest health status, using the Red Edge Position (REP) index and Structure-Insensitive Pigment Index (SITI), and showed a correlation between plant health and measured atmospheric dust depositions. Their results showed a statistically significant relationship between increased levels of elements associated with coal mining and combustion and decreased forest health.

At present, there have been no studies exploring the effects of air quality on urban vegetation via simultaneous measurements at high temporal frequency on the order of minutes for an extended temporal baseline of months. Therefore, in this work, we examine the temporal correlation between changes in air quality measures—namely, O_3, $PM_{2.5}$, temperature, and humidity—and the changes in the spectra of vegetation in ground-based, side-facing HSI images of an urban environment at high spatial, spectral, and temporal resolutions. In Section 2, we give a brief overview of remote sensing for vegetation health and then present our high-resolution HSI data and the method used for atmospheric correction, the air quality measurements used in this work, and the models used to quantify the correlation between the vegetation spectra and air quality. In Section 3, we present our results, we provide a discussion of their implications in Section 4, and summarize our conclusions in Section 5.

2. Materials and Methods

The literature on remote sensing of vegetation is dominated by the use of satellite, aerial, and, more recently, Unmanned Aerial Vehicle (UAV) imaging platforms. Satellite remote sensing platforms offer the benefits of enhanced spatial coverage and consistent data quality, making them cost-effective, particularly due to open access to a wealth of visible and multispectral data from some satellite platforms (e.g., Landsat 7–8) on which to base analyses [65]. However, satellite remote sensing also has its limitations, including the lack of high spatial resolution. For example, two of the most commonly used satellite datasets are Landsat and MODIS that have spatial resolutions of 30 m $\times$ 30 m and 500 m $\times$ 500 m per pixel, respectively. The coarse spatial resolution limits the ability to carry out precision urban agriculture studies, and makes the interpretation of vegetation health challenging when studying mixed canopies with a variety of species co-occurring with different phenological stages and health conditions [66]. Another limiting factor for satellite-based remote sensing is low temporal resolution, with "revisit time" for a given location typically on the order of days to several weeks (e.g., Landsat has an orbital period of 16 days). This is further exacerbated by potential obscuration by clouds, snow, and ice, that can yield revisits that stretch to months in some cases. The implication is that satellite remote sensing is useful for long-term phenological and land use studies, but lacks the temporal and spatial granularity to study the relationship between urban vegetation and environmental factors that can vary significantly over short spatial and temporal scales, on the order of meters and minutes, respectively, in urban areas. Airborne

and UAV platforms have the potential to solve some of these problems, however, due to the requirement of expensive aircraft and trained pilots, airborne platforms can be significantly cost prohibitive and, due to weather dependency, low data transfer speeds (particularly for high-resolution images), and legislative barriers for UAV platforms, neither is capable of collecting persistent data with high temporal granularity.

For the direct measurement of atmospheric and ecological variables at high spatial and temporal resolutions in forests and agriculture, "proximal sensing" by flux towers is normally employed. Flux towers are antenna-mounted arrays of multiple sensors that can observe temperature, humidity, atmospheric gases, atmospheric pollutants, and dust concentrations [67]. Flux towers have also been installed in urban areas to study issues such as the urban heat island effect, climate forecasting, air quality, and yardscape water demands and consumption [68]. However, to correlate these measurements with plant and vegetation health, studies either rely on indirect measurements such as evapotranspiration rates, or on using Photosynthetically Active Radiation (PAR) sensors which solely measure photosynthetic processes. To address these shortcomings, ground-based hyperspectral remote sensing has been employed over the past decade [69–71]. These near-surface ground-based hyperspectral cameras further add to vegetation health and phenology studies due to their ability to continuously retrieve images and spectra at a high temporal frequency, and on landscape or species spatial levels.

2.1. Hyperspectral Imaging Data

The Hyperspectral Imaging (HSI) data used in this work were obtained by the "Urban Observatory" (UO) facility in New York City (NYC) [71–74]. The UO has deployed broadband visible and infrared imaging cameras, as well as Visible and Near-Infrared (VNIR) and Long Wave Infrared (LWIR) HSI cameras that continuously image landscapes in NYC with high persistence and temporal resolution on the order of minutes. For this work, we use the VNIR instrument described in [73], a Specim Ltd. ImSpector V10E Visible Near-Infrared (VNIR) hyperspectral imager provided by Middleton Spectral Vision mounted atop a tall ∼120 m (∼400 ft) building in Brooklyn with a south-facing horizontal alignment. This instrument is a single slit scanning spectrograph with 1600 vertical pixels and is sensitive to 0.4 µm to 1.0 µm in 848 binned wavelength channels with a characteristic spectral resolution (full width half maximum) of 0.72 nm. The observations covered 30 days between 3 May and 6 June 2016. Each day, the instrument scanned the same scene every 15 min from 08h00 to 18h00. Scans with more than 5% of their pixels having more than 5% of their wavelengths saturated were discarded from the sample. A composite RGB image of the scene that maps the 0.61 µm, 0.54 µm, and 0.48 µm channels of one of the scans to the red, green, and blue values, respectively, is shown in Figure 1.

The scene shown in Figure 1 contains a variety of materials including sky, clouds, plant material, water, windows, concrete, bricks, metal structures, cars, and roads, and in this work we "segment" our HSI images to isolate those pixels corresponding to vegetation so that we can compare their temporal evolution with time series of air quality measures. Image segmentation of HSI data of dense urban areas is a difficult task given the complexity of the scene, particularly for side-facing images. Advanced deep learning algorithms have been developed and implemented to carry out this segmentation in the literature [75,76], however, as shown in [74], due to the uniqueness of the spectra of vegetation relative to all other urban materials, their identification is particularly robust across a variety of scenes and observational conditions, even with a single training instance when training a One-Dimensional Convolutional Neural Network (1D-CNN).

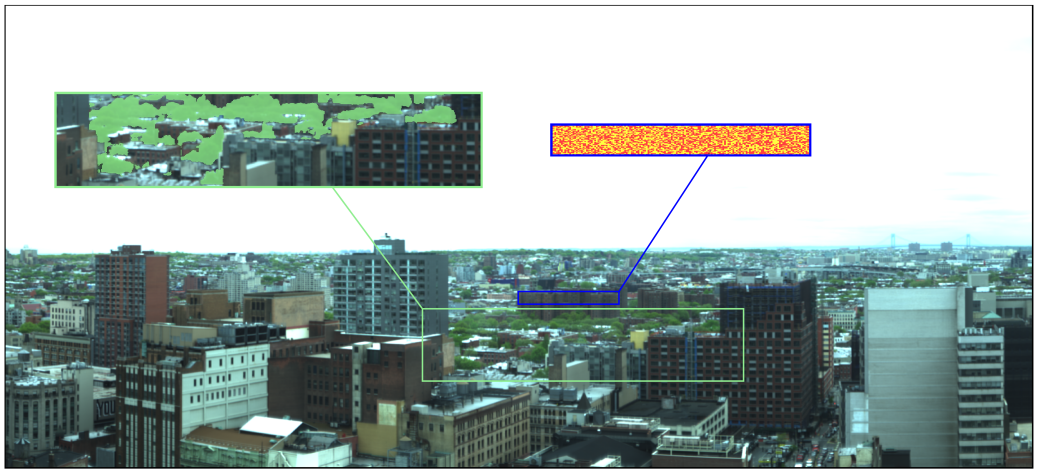

Figure 1. Full-resolution RGB (0.61 μm, 0.54 μm, and 0.48 μm) representation of the scene of Downtown and North Brooklyn imaged by the Urban Observatory's hyperspectral imaging system. The blue box shows the buildings used as controls, which were randomly split into two equal sets, represented by the red and yellow pixels in the expanded view. The green box shows the vegetation pixels (identified using *k*-means clustering and highlighted in the expanded view in green) whose spectra are used in this study.

In this work, we use a simple *k*-means clustering of pixel spectra to segment an image that had optimal uniform lighting and minimal shadowing into 10 clusters (we show below that the distinct nature of vegetation spectra results in performance that is comparable to more complex machine learning algorithms [77]). The resulting label map of the *k*-means clustering is shown in Figure 2 together with the mean spectra of pixels in the 10 clusters. The spectra of clusters 2 and 5 show the uniquely identifying features of vegetation; namely, the enhanced chlorophyll and leaf pigment reflectivity in the visible green peak range of ∼0.5–0.6 μm, absorption in the red range of ∼0.6–0.7 μm, the red edge at ∼0.7 μm, and high reflectance in near-IR due to spongy mesophyll in the plants' cellular structure. The green box in Figure 1 has an overlay of the pixels labeled as 2 and 5 by *k*-means in green to qualitatively show the accuracy of the unsupervised labeling. To demonstrate the robustness of this simple method for selection of vegetation pixels, we compare its performance with that of the 1D-CNN described in [74] for the scene in Figure 2. The performance of supervised machine learning models is often evaluated using "precision" and "recall". For a set of objects with known classifications, precision represents the fraction of classification predictions for which the model was correct, while recall represents the fraction of all instances of a given class that were correctly predicted by the model. Overall, while the CNN was far superior in identifying the various human-built and natural materials in the urban scene, both the CNN and *k*-means showed identical performance metrics for labeling *vegetation* pixels (precision = 1.00, recall = 0.98), with the mean vegetation spectra from both methods differing by <4% overall.

We note that the selection of vegetation pixels is not carried out for each HSI scan separately, but rather the pixels selected in Figure 2 are used in all scans in the observational campaign. This is justified by the fact that our HSI instrument is immobile and constantly observing the same scene, with pixel-level accuracy in the instrument pointing over the period of this study. Therefore, the pixels containing vegetation remain constant over all obtained images. Thus, the classification task need only be implemented once to label the pixels as either vegetation or non-vegetation before applying that labeling to all. Furthermore, as shown in [74], the same scene under less optimal lighting and cloud conditions can result in a measurable difference in classification accuracy. Repeating the *k*-means clustering for two other scans, one in the morning (08h31) and one in the afternoon (18h01) where both exhibit significant shadowing, the precision of the clustering of vegetation pixels remained at 1.00, however, the recall dropped to 0.70 and 0.68, respectively. Since the

accuracy of identification is variable while the pixels containing vegetation are constant across images, a single image taken at midday with optimal lighting and cloud conditions was chosen for segmentation.

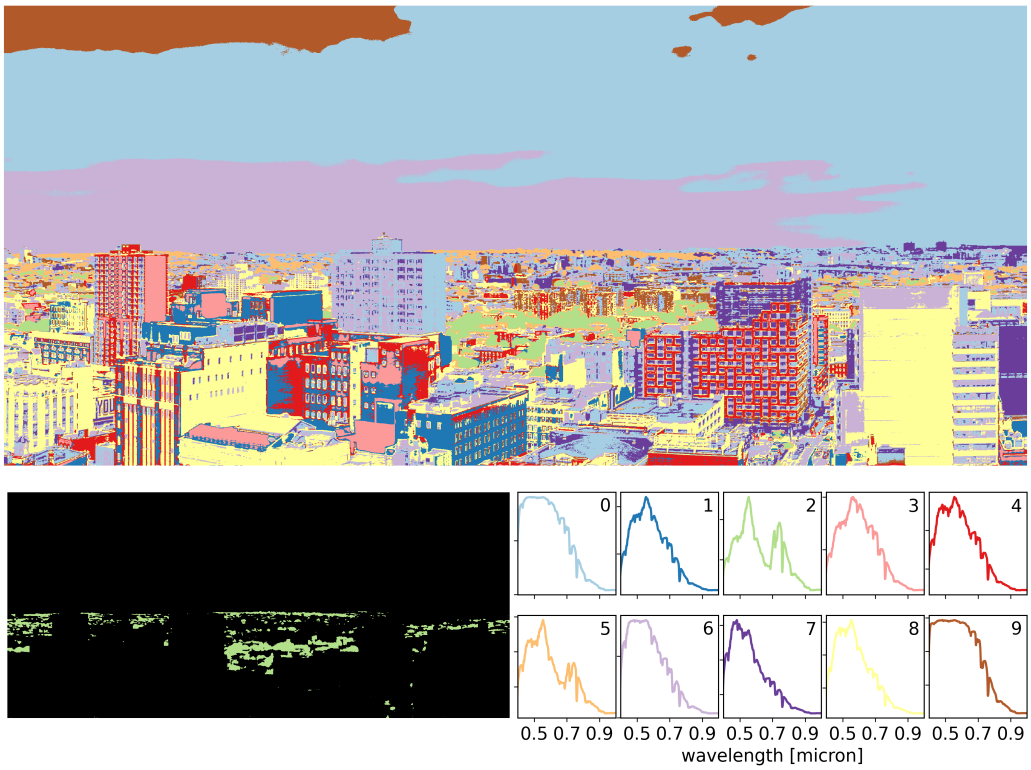

Figure 2. (**Top**): The cluster labels for a $k = 10$ k-means clustering of pixel spectra from the scene in Figure 1. An image of only pixels labeled as cluster 2 or cluster 5 is shown in the (**bottom left**). These cluster centers have spectra (**bottom right**) with enhanced green and near-infrared wavelengths, characteristic of chlorophyll reflectance, and so pixels labeled as belonging to those clusters are interpreted as vegetation.

2.2. Compound Ratio

In daytime hyperspectral imaging at Visible and Near-Infrared (VNIR) wavelengths of 0.4–1.0 µm, atmospheric interactions with solar radiation result in significant modifications to the spectrum received by the sensor as the light travels from the top of the atmosphere to the imaged object, and from the object to the sensor. Assuming emissions and surface reflectance are Lambertian [78], the geometric series expression for the radiance reaching the sensor ($L_{\lambda,t}$) at wavelength λ and time t can be expressed as:

$$L_{\lambda,t} = R_{\lambda,t} \cdot E_{\lambda,t} \cdot T_{\lambda,t} \tag{1}$$

where $R_{\lambda,t}$ is the surface reflectance, $T_{\lambda,t}$ is the total outward atmospheric transmission between the target and the sensor, and $E_{\lambda,t}$ is the total irradiance incident on the target, which is the contribution of solar irradiance and downward atmospheric transmission from the top of the atmosphere to the target. In the particular case of vegetation, due to plant fluorescence under solar illumination, there is an added weak emission with a magnitude of 2–5% of the reflected radiation in the near-infrared. This fluorescence ($F_{\lambda,t}$) is added as a perturbation to Equation (1) such that the radiance reaching the sensor from vegetation becomes a composition of two coupled contributions, the reflected ($R_{\lambda,t} \cdot E_{\lambda,t}$) and the emitted ($F_{\lambda,t}$) light:

$$L^V_{\lambda,t} = (R_{\lambda,t} \cdot E_{\lambda,t} + F_{\lambda,t}) \cdot T_{\lambda,t}. \tag{2}$$

With spectroscopic measurements of vegetation health via remote sensing, it is common to compute the apparent reflectance (R^*), which is the ratio between upwelling and incident fluxes, and accounts for the solar-induced fluorescence emission normalized by the irradiance incident on the target at surface level [78,79]:

$$R^*_{\lambda,t} = R_{\lambda,t} + \frac{F_{\lambda,t}}{E_{\lambda,t}}. \tag{3}$$

In order to obtain this apparent surface reflectance, it is imperative to account for and remove the effects of the atmosphere from the spectrum. Unlike satellite and aerial imaging, due to the orientation of ground-based HSI, the amount of atmosphere that light traverses prior to reaching the sensor varies significantly for each pixel. Therefore, correcting for atmospheric effects requires knowledge of observing geometries such as zenith and azimuth angles, sensor field of view, location of the Sun, and distance to each pixel, as well as atmospheric conditions and compositions, which may vary between the areas closer to the sensor and those at the horizon. Radiative transfer codes are commonly used in remote sensing applications to correct for atmospheric effects by modeling attenuation using assumed atmospheric conditions and concentrations and extracting surface reflectivity from the measured intensity by the sensor [80–82]. However, due to the oblique geometry of proximal remote sensing, the determination of the incident spectra is extremely difficult. In addition, given the varying distances of objects across the image from the sensor and the associated differences in atmospheric conditions across the image, atmospheric corrections with simulations of atmospheric effects can vary significantly across the image.

Therefore, in lieu of modeling the atmospheric effects, here we propose the use of a "*Compound Ratio*" for the analysis of vegetation spectra in urban environments that uses time-dependent comparisons of vegetation spectra with a nearby built structure to isolate the changes in vegetation apparent reflectance. In Figure 1, all the vegetation pixels inside the green rectangle are at an approximately uniform distance from the sensor. The buildings in the blue rectangle are at roughly the same location as the vegetation. Therefore, utilizing Equations (1) and (2), the mean at-sensor signal of the vegetation and building pixels can be expressed as:

$$V_{\lambda,t} = (R^V_{\lambda,t} \cdot E^V_{\lambda,t} + F_{\lambda,t}) \cdot T^V_{\lambda,t} \tag{4}$$

$$B_{\lambda,t} = R^B_{\lambda,t} \cdot E^B_{\lambda,t} \cdot T^B_{\lambda,t} \tag{5}$$

where $V_{\lambda,t}$ and $B_{\lambda,t}$ are the mean measured intensity of the vegetation and buildings (respectively) at wavelength λ and time t. By considering the following assumptions:

1. buildings have constant reflectivity over time, $R^B_{\lambda,t} = R^B_{\lambda,0} = R^B_\lambda$,
2. the total irradiance incident on the target is identical for buildings and vegetation, $E^V_{\lambda,t} = E^B_{\lambda,t} = E_{\lambda,t}$,
3. atmospheric transmission is identical for buildings and vegetation, $T^V_{\lambda,t} = T^B_{\lambda,t} = T_{\lambda,t}$.

Normalizing the intensities of each scan at t by the measured value at the start of the observing campaign $t = 0$ results in

$$V_{\lambda,t}/V_{\lambda,0} = \frac{(R^V_{\lambda,t} \cdot E_{\lambda,t} + F_{\lambda,t}) \cdot T_{\lambda,t}}{(R^V_{\lambda,0} \cdot E_{\lambda,0} + F_{\lambda,0}) \cdot T_{\lambda,0}} \tag{6}$$

$$B_{\lambda,t}/B_{\lambda,0} = \frac{R^B_\lambda \cdot E_{\lambda,t} \cdot T_{\lambda,t}}{R^B_\lambda \cdot E_{\lambda,0} \cdot T_{\lambda,0}} = \frac{E_{\lambda,t} \cdot T_{\lambda,t}}{E_{\lambda,0} \cdot T_{\lambda,0}}, \tag{7}$$

where the last equality follows from assumption 1 above and we have dropped the V and B superscripts on $E_{\lambda,t}$ and $T_{\lambda,t}$ due to assumptions 2 and 3 above. Dividing the normalized intensities of vegetation in Equation (6) by those of the buildings in Equation (7), we isolate

the *relative* change in the apparent reflectance of vegetation over time by defining the *Compound Ratio* of vegetation $C^V_{\lambda,t}$:

$$C^V_{\lambda,t} \equiv \frac{V_{\lambda,t}/V_{\lambda,0}}{B_{\lambda,t}/B_{\lambda,0}} = \frac{R^V_{\lambda,t} + (F_{\lambda,t}/E_{\lambda,t})}{R^V_{\lambda,0} + (F_{\lambda,0}/E_{\lambda,0})} = \frac{R^{*,V}_{\lambda,t}}{R^{*,V}_{\lambda,0}}. \quad (8)$$

It is important to note that vegetation reflectance is affected by the angle of the incoming spectrum due to factors that include leaf orientation and sun-sensor geometry [83,84]. However, the formulation above implicitly assumes that reflectance is independent of the angle of incoming radiation. While this may result in residuals that can impact the accuracy of the Compound Ratio, integrating the spectrum of vegetation over the entire canopy within the green box in Figure 1 minimizes this effect. To provide a control sample demonstrating the soundness of the Compound Ratio assumptions, the pixels of the buildings in the blue box in Figure 1 were randomly split into the two sets represented by the red and yellow labels shown. This allows us to calculate both the Compound Ratio of vegetation-to-buildings ($C^V_{\lambda,t}$) from Equation (8) using one set of building pixels, as well as the Compound Ratio of buildings-to-buildings ($C^B_{\lambda,t}$) using the two sets of randomly split building pixels. If all the assumptions listed above hold true, it is then expected that the Compound Ratio of buildings-to-buildings should result in a constant value of 1 in both wavelength and time dimensions. Furthermore, as seen in Figure 2 the building used for the control is composed of several human-built materials with slightly different spectra. By randomly splitting the building pixels into two sets, we minimize the allocation of any one single material to each set and maximize the likelihood that the Compound Ratio of building-to-building would capture the changes in apparent reflectance of the building rather than the change in one particular spectrum of one material relative to another. Figure 3 shows a mapping of the Compound Ratios of vegetation and buildings for all wavelengths and scans in the top row, while the bottom row shows the Compound Ratios of 10% of scans, randomly selected and plotted as functions of wavelengths. Noting the difference in scaling of the color-bars in each mapping as well as the y-axis of the bottom plots, it is evident that the assumption of lack of reflectivity holds true for buildings as the amplitude of change in Compound Ratios of buildings is dominated by noise that is varying at the ∼1% level. On the other hand, the Compound Ratio of vegetation shows *variation over time* in the green peak of chlorophyll, the red edge, absorption in red, and emission in near-infrared, all unique identifiers of the vegetation spectrum. These variations reach the ∼50% level, which is in line with previous studies [85,86]. Thus, we find that the plant reflectivity itself is changing on 15 min time scales.

It is worth noting that in the Compound Ratios of vegetation in Figure 3, there is visible absorption occurring at wavelengths ∼0.76–0.77 µm. The instrument used in this work does not exhibit sharp wavelength-dependent sensitivity that would cause such a feature. Therefore, it is likely to result from residual A-band absorption of oxygen in the atmosphere. The presence of atmospheric absorption following the previously mentioned treatment to remove atmospheric effects is indicative that the assumptions may not be absolute. Dirt, moss, and sticking of pollutants to the surfaces of buildings affect assumption 1. Furthermore, assumptions 2 and 3 require that the vegetation and comparison buildings are at the exact same location, thus, any deviation can cause the depth of the atmosphere as well as amount of incident light to differ between the two objects and result in residual atmospheric effects in the final Compound Ratio. Moreover, the Compound Ratio of buildings in Figure 3 shows small illumination variations in the visible portion of the spectrum from ∼0.45–0.7 µm that resemble the residual from the solar spectrum. However, given the small magnitude of changes in building Compound Ratios we can be confident that changes seen in the Compound Ratios of vegetation are far more likely to be due to changes in vegetation reflectivity rather than atmospheric effects, especially considering that the varying features are all characteristic of vegetation spectra. Further investigation

into the soundness of using the building as atmospheric irradiance and transmission control for the vegetation is presented in Appendix B.

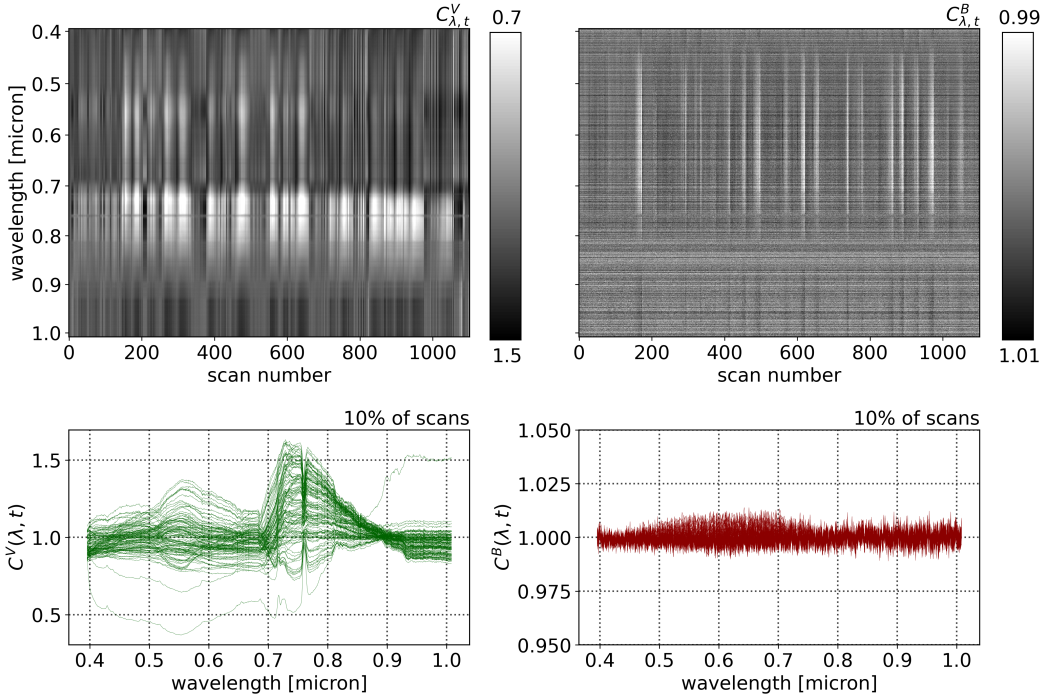

Figure 3. (**Top**): Compound Ratios of all scans for vegetation (**left**) and building (**right**) pixels as functions of wavelength and scan number (i.e., time). (**Bottom**): Compound Ratio of 10% of scans from Figure 3 for vegetation pixels (**left**) and building pixels (**right**) as a function of wavelength. Note that vegetation reflectances are varying at ∼50% relative to a set of nearby building pixels, while the building pixels are only varying at ∼1% relative to each other.

2.3. Air Quality Measurements

For the purpose of this work, we use measurements of O_3 and $PM_{2.5}$ concentrations, temperatures, and humidity (air moisture content). We use temperatures and relative humidity measurements from available Weather Underground data (https://www.wunderground.com/, accessed on 6 June 2016) for the location, days, and times of our HSI scans. Relative humidity was then converted to absolute humidity (mass of water vapor per unit volume of air, g/cm^3) using the general law of perfect gases, the specific gas constant for water vapor, and assuming 1 atm pressure. For the O_3 and $PM_{2.5}$ concentrations at the times of our scans, we use the openly available New York State Department of Environmental Conservation (NYS DEC) data. The locations of the NY DEC's air quality monitoring sites, and the approximate locations of the Weather Underground crowdsourced network of air quality sensors, are shown in Figure 4 together with the location of the vegetation and buildings used in this study, and a summary of the data obtained from each source is shown in Table 1. For obtaining the individual air quality measures used in this study for each scan, we took the average O_3, $PM_{2.5}$, temperature, and humidity at each scan time over a large area, including outside the near vicinity of our selected vegetation and buildings. Although the sensor network is distributed over a large area and not directly adjacent to the vegetation patch under study, we take the average values for several reasons. It is well known that individual air quality sensors require precise and periodic calibration and tend to be noisy [87,88], especially in the presence of the urban island heat effect and localized emissions in urban environments [89,90]. Although calibration of the sensor network is outside the scope of this paper, averaging multiple measurements from different sensors can reduce the impact of noise on the individual measurement. Furthermore, as evident in Figure 4, there are no air quality monitoring sites directly atop or adjacent to our imaged

vegetation and buildings. Averaging the surrounding measurements allows us to extract a relatively accurate representation of the air quality values of our given location.

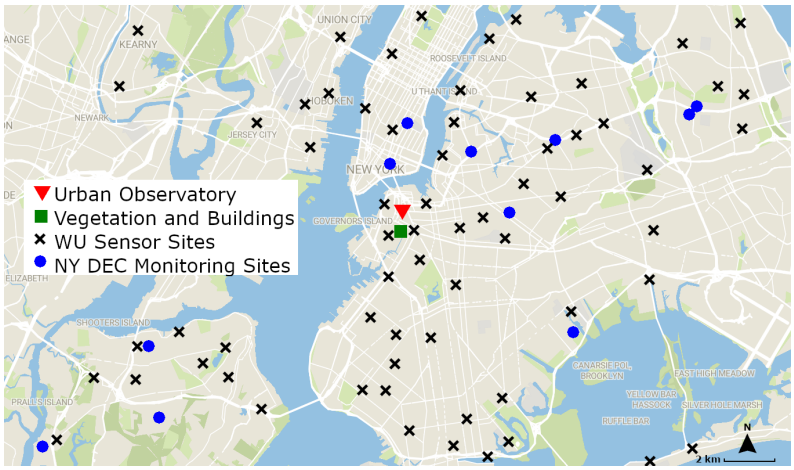

Figure 4. Map of NYC showing the locations of the Urban Observatory's hyperspectral imaging system (red triangle), the vegetation and buildings used in this study (green square), the New York State Department of Environmental Conservation's air quality monitoring sites (blue circles), and the Weather Underground network of air quality sensors (black crosses).

Table 1. Collected variables from the observation sites shown in Figure 4.

Site	Observed Variable	Details
New York State Department of Environmental Conservation (NYS DEC)	Temperature	Obtained in F and converted to °C
	Humidity	Obtained as relative humidity and converted to absolute humidity in g/cm^3
Weather Underground (WU)	Ozone (O_3)	Concentration in ppm
	Particulate matter ($PM_{2.5}$)	Concentration in $\mu g/m^3$
Urban Observatory (UO)	Hyperspectral images	Obtained in data cubes of 1600×1600 pixels, each pixel containing a spectrum in 848 binned wavelength channels between 0.4 µm and 1.0 µm

Figure 5 shows the four air quality parameters for each scan time in a scatter matrix (scan times with precipitation or 100% relative humidity were removed from the sample to eliminate any effects of rain drops near the camera). It is worth noting that there is a visible correlation between ozone and temperature. The figure also shows the four air quality parameters after standardization ($\mu = 0, \sigma = 1$) plotted as functions of scan number, where it is further evident that O_3 and temperature exhibit correlated changes with time. Studies over multiple time scales have shown that there is a strong correlation between surface temperature and O_3 concentrations [34–36], with temperatures having a correlation coefficient up to ~80% when used to estimate ozone concentrations in urban environments [91]. This correlation becomes more complex with $PM_{2.5}$ where studies have shown that a positive correlation between $PM_{2.5}$ and O_3 exists at high temperatures, and a negative correlation at lower temperatures [92]. Furthermore, temperature inversion and the mixing of atmospheric layers can have a significant impact on O_3 and $PM_{2.5}$ concentrations as well as humidity [37,38], which adds further complexity to their correlations and covariances.

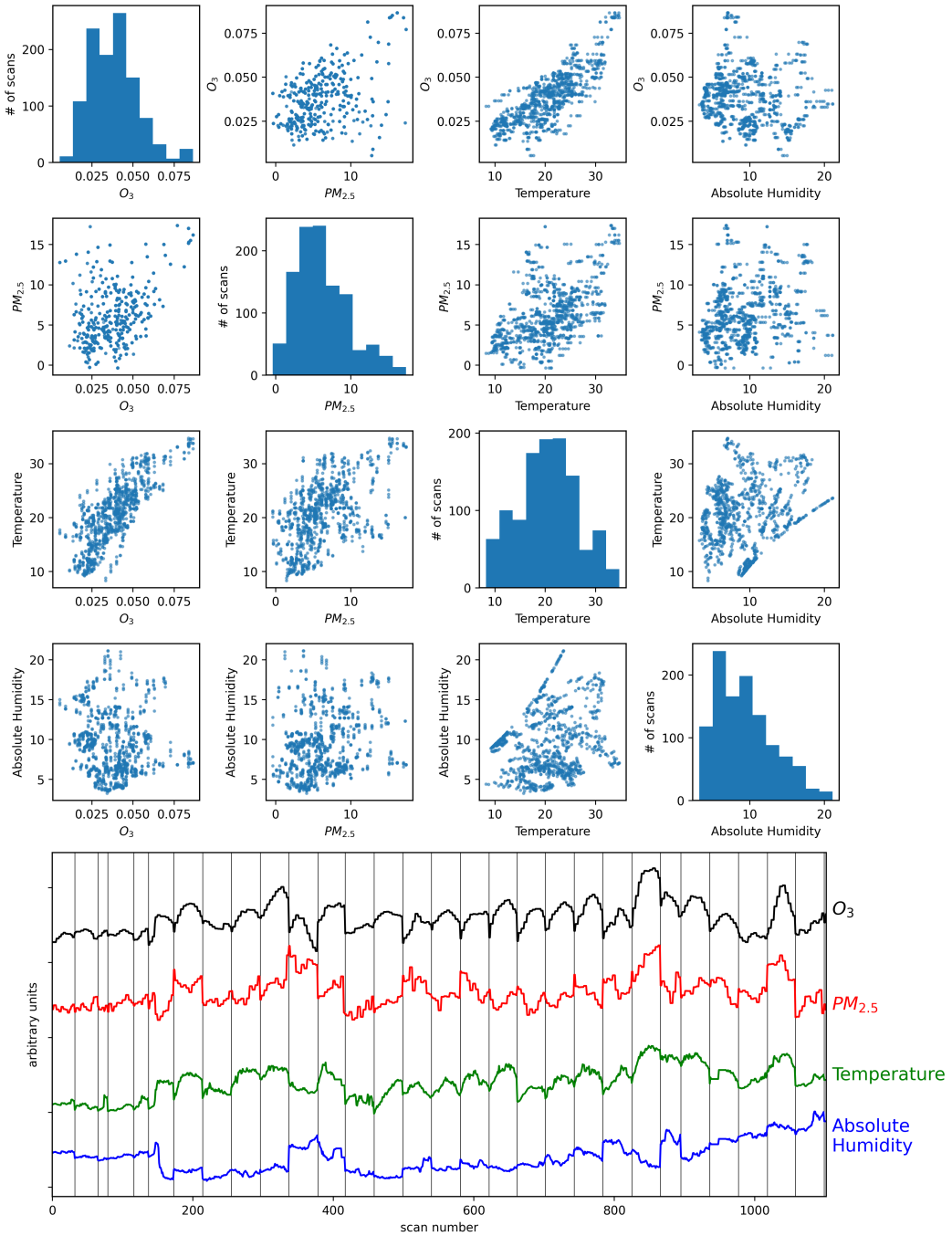

Figure 5. (**Top**): Air quality scatter matrix showing the distribution of O_3 (in ppm) and $PM_{2.5}$ (in $\mu g/m^3$) concentrations, temperature (in °C), and absolute humidity (in g/cm^3). (**Bottom**): Normalized and offset O_3 and $PM_{2.5}$ concentrations, temperature, and absolute humidity as a function of scan number. Vertical lines indicate the change in days.

2.4. Tracers of Vegetation Health

The concept of utilizing the leaf optical responses to study the impact of various stresses on vegetation health has been used widely in the remote sensing field [59,93,94]. The justification behind using the spectral wavebands from 400–2500 nm as predictors of plant health is that unfavorable conditions result in morphological and physiological changes in plants that disturb the processes of transpiration and photosynthesis and, therefore, impact the manner with which the plants interact with light. The part of the spectrum in the visible wavelengths from 400–700 nm is primarily influenced by colored pigments

such as chlorophyll and carotenoids [95–97], while the 700–1400 nm range reflects leaf structural characteristics [98], and 1400–2500 nm is mainly affected by the tissue water content [99]. Due to the central role of chlorophyll in the process of photosynthesis, chlorophyll content is often used as an indicator for plant physiological health [100,101]. Aside from chlorophyll, carotenoids, including α- and β-carotenes and xanthophylls, are the other main pigments of green leaves with particular physiological functions related to photosynthesis. Visually, reductions in chlorophyll are perceived as yellowing of leaves primarily due to the relative increase in carotenoid content [102], which are retained during leaf senescence as a mechanism of photoprotection. Therefore, changes to carotenoid content and their proportion to chlorophyll content are also widely used as indicators of physiological and health status in plants [96,103]. Other common indicators of physiological and morphological changes detectable in the spectra of vegetation and used as cues for changes in plant health include leaf dry matter content, also known as leaf mass [99,104], leaf water equivalent layer [105,106], and leaf senescence [61,107].

The Soil Canopy Observation of Photosynthesis and Energy fluxes (SCOPE) model couples photosynthetic, hydrological, and radiative transfer models to provide simulations of hyperspectral radiance and net radiation, photosynthesis rates, and various heat fluxes for soil, leaves, and vegetation canopies [108,109]. Using SCOPE to simulate the apparent reflectance of vegetation with varying morphological and physiological properties allows for the demonstration of the aspects of the proposed Compound Ratio that correspond to tracers of vegetation health. Vegetation with varying chlorophyll AB content (C_{ab}), carotenoid content (C_{ca}), dry matter content (C_{dm}), leaf water equivalent layer (C_w), and senescent material fraction (C_s) has spectra that reflect different health statuses. Figure 6a shows the SCOPE simulations of the apparent reflectance (R^*)—which includes the fraction of radiation in the observation direction (R) with the added ratio of emitted fluorescence to irradiance (F/E)—produced by varying the aforementioned indicators of physiological and health status in plants. The ability to utilize the spectra of vegetation to extract information regarding their health is exemplified by the significant changes in the simulated spectra when varying their physiological and morphological status indicators. The Compound Ratio as presented in Section 2.2 is essentially the rate of change in apparent reflectance. Figure 6b shows the Compound Ratio computed for the simulated apparent reflectances by considering one of the simulations as being $R_{\lambda,0}$ (the apparent reflectance at time $t = 0$) to use as the denominator of Equation (8), which demonstrates the ability of the proposed Compound Ratio to reflect the changes in the health status of vegetation.

For this work, we rely on two methods for quantifying vegetation health from its Compound Ratio spectra: a simple ratio of the wavelength where solar-induced fluorescence peaks relative to a control wavelength, and the amplitudes of a Principal Component Analysis (PCA) decomposition that captures variation in the entire spectrum of a given scan.

2.4.1. Solar-Induced Fluorescence (SIF)

Solar-Induced chlorophyll Fluorescence (SIF) has a functional connection with photosynthesis and an insensitivity to atmospheric scattering, and has therefore been proven to be an effective signal for monitoring vegetation physiology with significant advantages over other remote sensing indicators [110,111]. Photosynthetically active energy absorbed by vegetation can be used in photochemical reactions, re-emitted as fluorescence, or dissipated as heat, and any efficiency change in one of these processes results in alterations in the remaining two. Therefore, unlike commonly used indices that rely on reflectance-based parameters such as the Normalized Difference Vegetation Index (NDVI) or the Photochemical Reflectance Index (PRI), SIF is a byproduct of photosynthesis and an indicator of Gross Primary Production (GPP) [112,113]. Since SIF contains information on Photosynthetically Active Radiation (PAR), it has been used as a strong indicator for photosynthesis, and gives a measure of plant stress responses to changes in temperature, water availability, nutrients, and other environmental and health factors [114,115]. Figure 6c shows the SIF spectrum for the SCOPE simulated vegetation spectra with varying levels of C_{ab}, C_{ca}, C_{dm}, C_w, and C_s

which reflect the ability to infer the health of the plants from the changes in the levels of SIF. Furthermore, by integrating the fluorescence spectra to obtain the area under the SIF curve, Figure 6d shows the strong correlation between solar-induced fluorescence and photosynthesis rates in vegetation with a Pearson's correlation coefficient of 0.84.

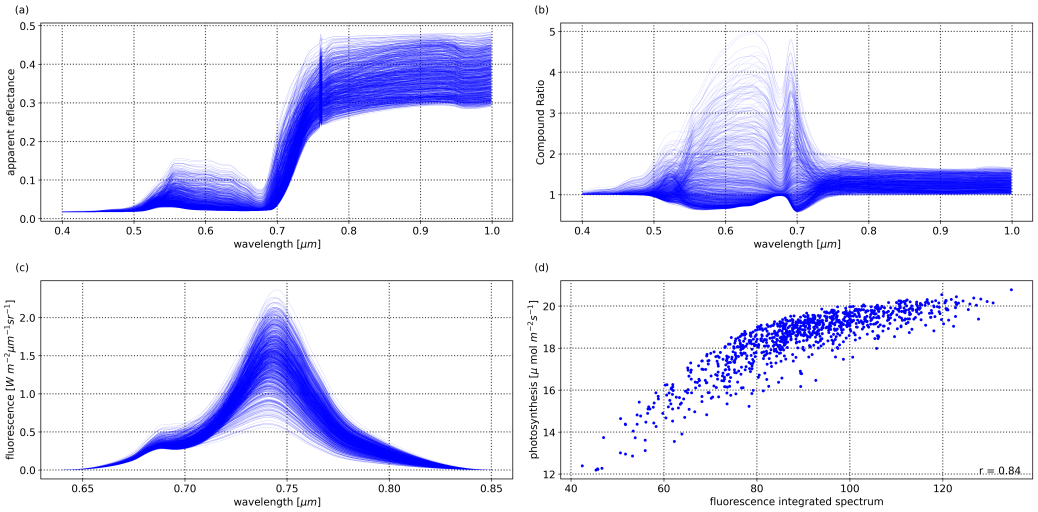

Figure 6. SCOPE model simulations with varying chlorophyll AB content (C_{ab}), carotenoid content (C_{ca}), dry matter content (C_{dm}), leaf water equivalent layer (C_w), and senescent material fraction (C_s), showing (**a**) the apparent reflectance spectrum (R^*), (**b**) the Compound Ratio ($C^V_{\lambda,t}$) computed using Equation (8), (**c**) the fluorescence emitted per wavelength in observation direction, and (**d**) photosynthesis as a function of the area under the fluorescence curve.

There are two major methods with which SIF is quantified: radiance-based and reflectance-based methods. Radiance-based methods depend primarily on exploiting the narrow absorption feature of the Fraunhofer line for telluric oxygen (O_2A) at 760.4 nm to isolate SIF from the reflected spectrum, which allows for the estimation of SIF in physical radiance units if the data are calibrated. The majority of radiance-based methods in the literature essentially derive from the Fraunhofer Line Depth (FLD) principle, initially proposed by [116,117]. The FLD method relies on two measurements of the radiance, one inside and one outside the O_2 Fraunhofer absorption bands, where the magnitude of SIF is computed by comparing the magnitude of the measured signals. In essence, FLD methods require knowledge of the incident solar irradiance (E in Equation (2)) and target radiance (L in Equation (2)) at wavelengths in the bottom and shoulder of the absorption feature in order to solve for the magnitude of fluorescence under the assumption that Reflectance (R) and Fluorescence (F) are constant at the two wavelengths. Refinements and enhancements to this method have been introduced, including the three-channel FLD (3FLD) [118], FLD with correction factors (cFLD) [119], and improved FLD (iFLD) [120], all of which follow the same principle with modifications. More sophisticated methods for retrieving the full SIF spectrum generally rely on either Spectral Fitting Methods (SFMs) which do not rely on the assumption of constant reflectance and fluorescence such as the Fluorescence Spectrum Reconstruction (FSR) [121], or model inversion approaches [122].

Reflectance-based methods, on the other hand, rely on the effects of fluorescence on the apparent reflectance spectrum in the red-edge region rather than the Fraunhofer line. While radiance-based approaches generally produce measurements of fluorescence with physical units, reflectance-based methods rely on computing indices that actually reflect vegetation physiological changes that are strongly correlated with the same processes responsible for changes in fluorescence (as opposed to tracking the fluorescence emissions themselves). Since SIF extends over the wavelength range of 640 to 850 nm, with a broad peak centered at 750 nm and a smaller peak near 690 nm [123], these indices are computed using the apparent reflectance at a wavelength affected by fluorescence (typically around

one of the two fluorescence maxima at 690 and 750 nm) compared to another that is less or not affected by fluorescence. Some examples of the use of reflectance-based indices include R^*_{690}/R^*_{600}, R^*_{740}/R^*_{800}, R^*_{750}/R^*_{800}, R^*_{685}/R^*_{655}, and R^*_{690}/R^*_{655}, as well as curvature indices such as $(R^*_{685})^2/(R^*_{675} \cdot R^*_{690})$ [123–129]. While a full decoupling of the fluorescence effects from the apparent reflectance cannot be achieved using these methods, the normalization of the reflectance using ratios optimizes the indices that are sensitive to changes in fluorescence and have an advantage over radiance-based approaches by not requiring complex processing and knowledge of various fluxes and parameters.

As shown in Section 2.2, the Compound Ratio is computed in our data from the radiance received at the sensor in order to isolate the changes in apparent reflectance of vegetation from the atmospheric transmission and incident irradiance on the target. In Figure 3, changes in the Compound Ratio at wavelength ∼0.75 µm can visibly be matched with concurrent changes in air quality parameters for similar scans in Figure 5. On the other hand, the Compound Ratio at wavelengths of 0.9 µm presents relatively little to no variation with time. Given these observations, and the fact that the Compound Ratio is a measure of the change in reflectance rather than radiance, we employ a reflectance-based approach and measure the variation in fluorescent emissions by using a Solar-Induced Fluorescence indicator ($SIFi$) computed as a simple ratio of the amplitude of the Compound Ratio at 0.75 µm relative to that of the less affected reference at 0.9 µm as:

$$SIFi_t = \frac{C_{0.75,t}}{C_{0.9,t}}. \tag{9}$$

Using the SCOPE simulated spectra in Figure 6, the SIF indicator was calculated using Equation (9), with the values shown for various parameter values in Figure 7. Provided that the Compound Ratio is the relative change in reflectance, we also compute the relative change in the various vegetation parameters from the output of SCOPE (ΔC_x, such that x is ab for chlorophyll AB content, ca for carotentoid content, etc.) by considering one simulation to be the parameter at time 0, and computing the change in each C_x in the same manner shown in Equation (8). In Figure 7a, there is a clear correlation between the SIF indicator and the change in fluorescence quantified by integrating the simulated fluorescence spectra in Figure 6c with a Pearson's correlation coefficient (r) of 0.72. Given the input parameter values, it is evident that these correlations are primarily driven by changes in chlorophyll AB content ($r = 0.88$), with a weaker influence by dry matter content ($r = -0.34$) and relatively no impact from carotenoid content, leaf water equivalent layer, or senescent material fraction. Given the relation between fluorescence and photosynthesis rate as seen in Figure 6d, this correlation also translates into a strong correlation between the SIF indicator and the change in photosynthetic rate seen in Figure 7b ($r = 0.86$) and shows that it is reasonable to use this indicator as a tracer of vegetation health.

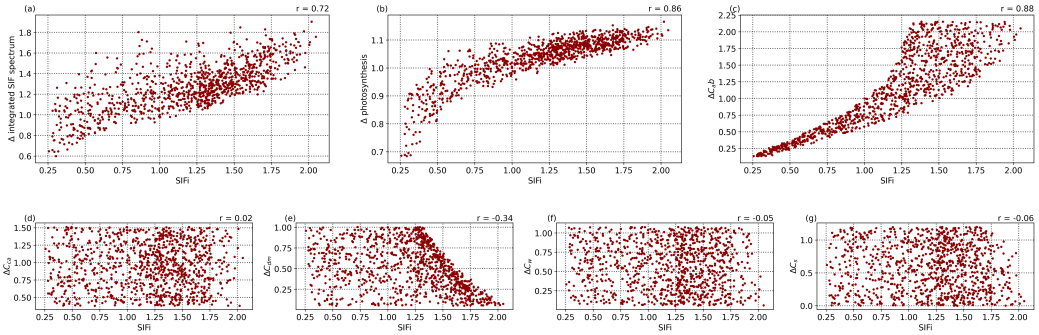

Figure 7. SCOPE simulations showing the correlations between the SIF indicator values calculated using Equation (9) and relative changes in: (**a**) the integrated solar induced fluorescence spectra, (**b**) photosynthesis rates, (**c**) chlorophyll AB content (C_{ab}), (**d**) carotenoid content (C_{ca}), (**e**) dry matter content (C_{dm}), (**f**) leaf water equivalent layer (C_w), and (**g**) senescent material fraction (C_s).

2.4.2. Principal Component Analysis (PCA)

Vegetation indices that use linear or ratio combinations of various wavelengths selectively indicate stress conditions in a particular domain; for example, indices based on the red edge such as NDVI and RDVI [130] represent a measure of leaf chlorophyll content, while xanthophyll-related indices such as PRI focus on the green peak. However, the full vegetation spectrum from 0.4–1.0 µm contains information on pigments, cellular biochemicals (proteins, lignin, cellulose), and water leaf content, among various other indicators of plant health. Therefore, hyperspectral imaging provides a wealth of information on the status of vegetation throughout the VNIR wavelength range. Using the entire spectrum rather than a few narrow bands has the potential to offer a more holistic approach to capturing the health of vegetation. On the other hand, hyperspectral images are known to contain redundant information, and so Principal Component Analysis (PCA) decomposition is commonly used in hyperspectral analyses to reduce dimensionality by removing such redundant information while encoding global spectral information important for identifying vegetation health in a set of characteristic spectra [131,132]. In our case, PCA uses correlated spectral attributes of the Compound Ratio spectra at the various time steps to determine an orthogonal basis set of N Principal Component (PC) spectra that describe the principal variability in them. Using $N = 4$ results in principal components that explain a total of >99% of the variability in the vegetation's Compound Ratio spectra, and any additional components yield relatively insignificant explained variances (<0.5%). Figures 8 and 9 show the PCA decomposition of the vegetation and building spectra, respectively, where the explained variances for the components in vegetation are 70.5%, 24.8%, 2.6%, and 1.4%, while those of the buildings are 42.1%, 0.9%, 0.4%, and 0.3%. We note that their shapes clearly show the dominance of noise in the composition of the spectrum of buildings.

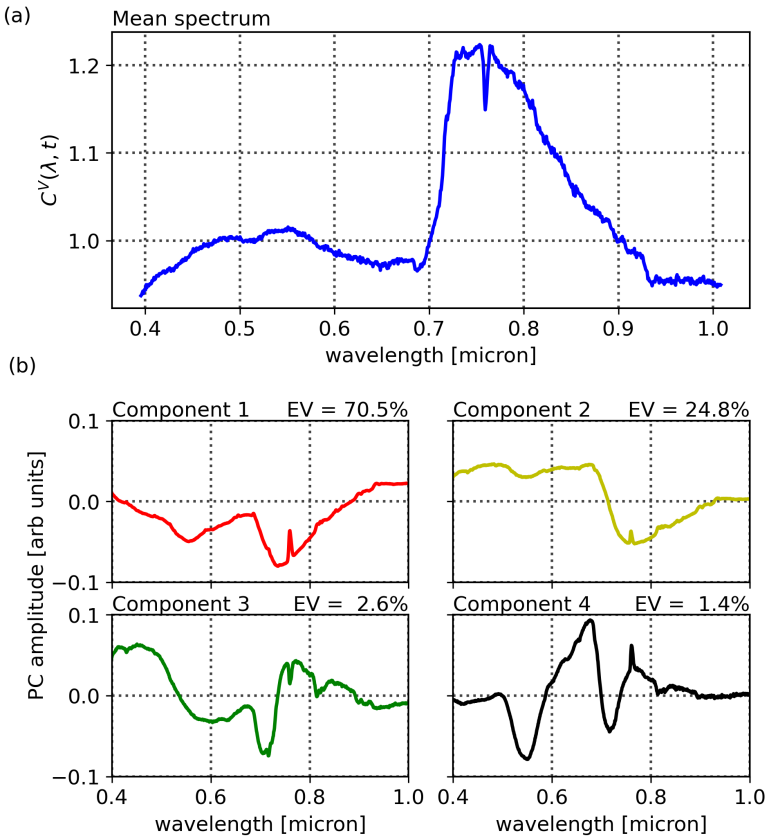

Figure 8. (**a**) The mean Compound Ratio spectrum of vegetation pixels. (**b**) The amplitude of each of the 4 principal components as functions of wavelength and their Explained Variance (EV) in %.

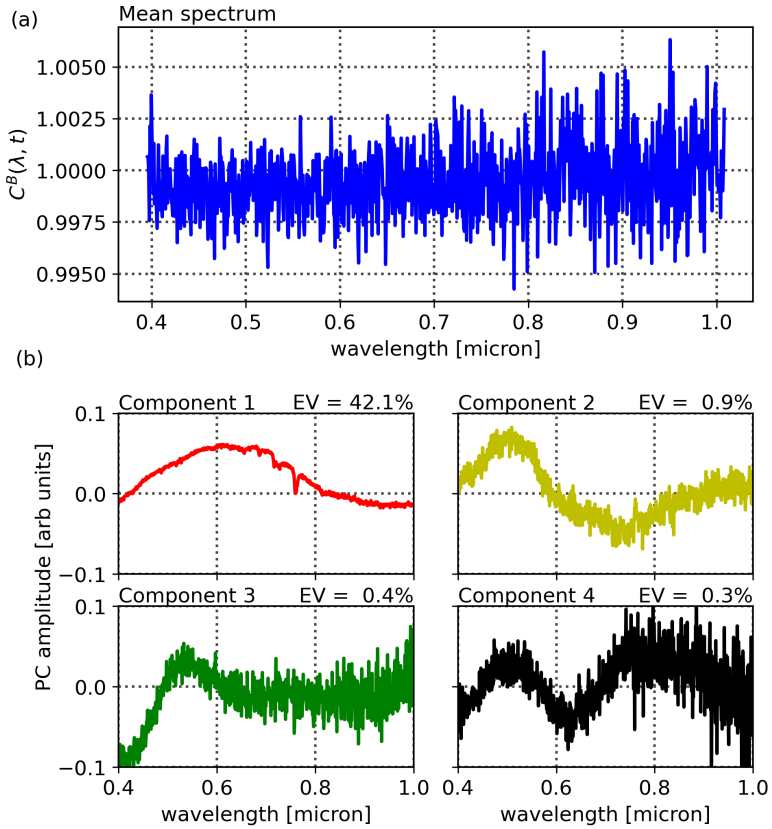

Figure 9. (**a**) The mean Compound Ratio spectrum of building pixels. (**b**) The amplitude of each of the 4 principal components as functions of wavelength and their Explained Variance (EV) in %.

Dimensionality is reduced by projecting each 848-channel Compound Ratio spectrum onto the N components and, as we describe in Section 3.2, it is the variability in those projected amplitudes that is compared with air quality variability. This variability in amplitudes in essence is a measure of the variations in vegetation spectra, and given that changes in the health of vegetation result in variations in their spectra proportional in magnitude to changes in health status, it follows that the variability in projected amplitudes is representative of vegetation health. To test this claim, we performed the same PCA decomposition on the Compound Ratio spectra calculated from the SCOPE simulated apparent reflectances in Figure 6. In the same manner as in Section 2.4.1, we explore the correlation between the various principal component amplitudes and the parameters of the model and show their correlation coefficients in Table 2. Principal component 1 shows a significant inverse correlation with the change in the rate of photosynthesis ($r = -0.82$) and the chlorophyll AB content ($r = -0.84$). Principal component 2 exhibits a weaker correlation with photosynthesis rate ($r = 0.35$), but shows a significant inverse correlation with dry matter content ($r = -0.92$). Principal component 3 shows levels of correlation with photosynthesis ($r = 0.24$), chlorophyll AB content ($r = -0.26$), dry matter content ($r = 0.22$), and senescent material fraction ($r = -0.30$), but it also exhibits stronger correlation with carotenoid content ($r = -0.57$). Lastly, component 4 shows only a weak correlation with chlorophyll AB content ($r = 0.27$), and stronger correlation with carotenoid content ($r = -0.69$).

Table 2. Pearson's correlation coefficients between the PCA component amplitudes of the Compound Ratio spectra calculated from the SCOPE simulated apparent reflectances and relative changes in the various vegetation health indicators: photosynthesis rates, chlorophyll AB content (C_{ab}), carotenoid content (C_{ca}), dry matter content (C_{dm}), leaf water equivalent layer (C_w), and senescent material fraction (C_s.)

	Δ Photosynthesis	**ΔC_{ab}**	**ΔC_{ca}**	**ΔC_{dm}**	**ΔC_w**	**ΔC_s**
PCA 1	−0.82	−0.84	−0.04	−0.05	0.03	−0.09
PCA 2	0.35	0.02	−0.02	−0.92	−0.08	−0.33
PCA 3	0.24	−0.26	−0.57	0.22	0.06	−0.30
PCA 4	0.10	0.27	−0.69	−0.09	0.00	0.12

2.4.3. Linear Model

To explore the dependence of these vegetation health indicators on air quality, we model each indicator as a simple linear function of the air quality parameters:

$$f_t = \vec{w} \cdot \mathbf{P} \quad (10)$$

$$\mathbf{P} = (\vec{O_3}, \vec{PM_{2.5}}, \vec{T}, \vec{H}, \vec{1}), \quad (11)$$

where f_t is the quantified vegetation health measure extracted from the Compound Ratio spectra as a function of time and represents both the SIF indicator ($SIFi$) as seen in Section 3.1 and PCA component amplitudes in Section 3.2, $\vec{w}$ is a vector containing the air quality parameter coefficients, and **P** contains the normalized measured O_3, $PM_{2.5}$, temperature (T), and humidity (H) as functions of time together with a constant. Markov Chain Monte Carlo (MCMC) sampling, implemented with the EMCEE package in Python [133], is used to estimate the probability distribution of the parameters $\vec{w}$ in each model. This MCMC approach generates samples of the likelihood function, which we define here as

$$\ln p(y|t, \vec{w}, \varepsilon) = -\frac{1}{2} \sum_t \left[\frac{(y_t - f_t(\vec{w}))^2}{\varepsilon_t^2} + \ln(2\pi\varepsilon_t^2) \right], \quad (12)$$

where y is the observed quantified vegetation health measure extracted from the spectra as a function of time and ε represents an amount by which the noise is underestimated. By generating sufficient samples of the posterior surface, the maximum likelihood and (fully covariant) uncertainties for the air quality parameter coefficients $\vec{w}$ are determined.

3. Results

As described in Section 2.4 above, our primary results are derived by comparing two methods for quantifying vegetation health—an SIF indicator composed of the simple ratio of Compound Ratios at 0.75 and 0.9 µm and projected amplitudes from PCA decomposition—with air quality indicators over time. For a comparison with other commonly used vegetation indices that address different parts of the spectrum, we also present the use of NDVI and PRI in Appendices A.1 and A.2, respectively.

3.1. Solar-Induced Fluorescence Indicator (SIFi)

The Solar-Induced Fluorescence indicator ($SIFi$) (ratio of Compound Ratios at 0.75 and 0.9 µm) was calculated for both the vegetation and buildings in Figure 1 at each scan time using the full spectral resolution of 848 spectral channels. This time series was standardized across time steps to have $\mu = 0$ and $\sigma = 1$. Figures 10 and 11 show the resulting full posterior distributions of the linear coefficients for the atmospheric variables after MCMC sampling, as described in Section 2.4.3. Both figures also show the standardized $SIFi$ values plotted as functions of scan number, and a 10% sample of the possible models using the parameters' coefficients produced by MCMC. The median values for the atmospheric

parameter coefficients are summarized in Table 3 together with their fully covariant 3σ ranges of uncertainty that are calculated using the 3σ contours in the posterior distributions provided in the corner plots in Figures 10 and 11. We note the importance of utilizing the full covariance to compute the uncertainties, particularly in the case of the temperature and ozone, which exhibit strong covariance and would result in significant underestimation of uncertainty if calculated using the cross-sections of the contours without regard to the full covariance.

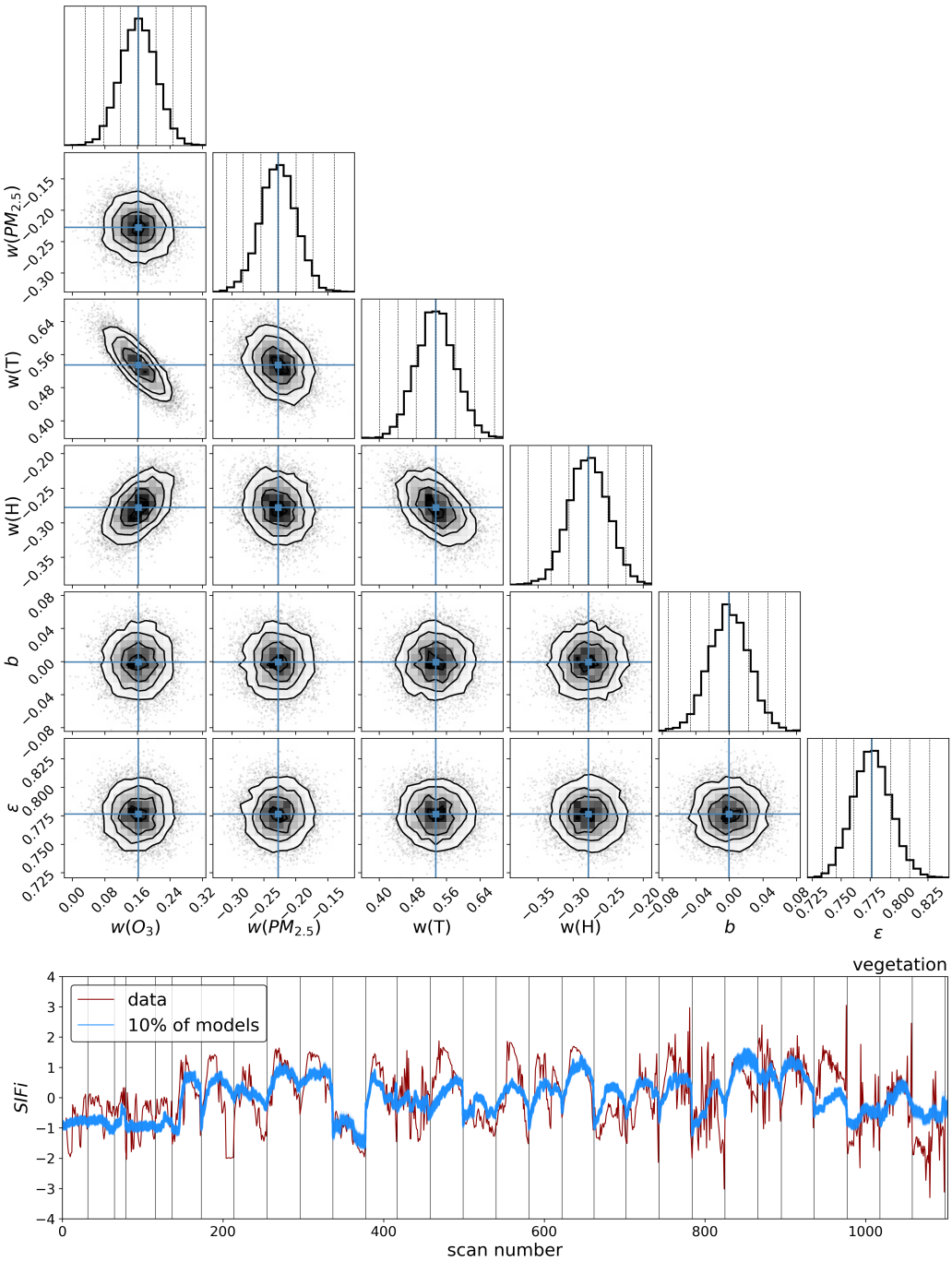

Figure 10. (**Top**): MCMC corner plot of the posterior distribution of air quality parameters for vegetation. (**Bottom**): The measured SIF indicator (*SIFi*) values as a function of scan number with 10% of randomly selected models from those identified as probable by MCMC, with the vertical lines indicating the change in days.

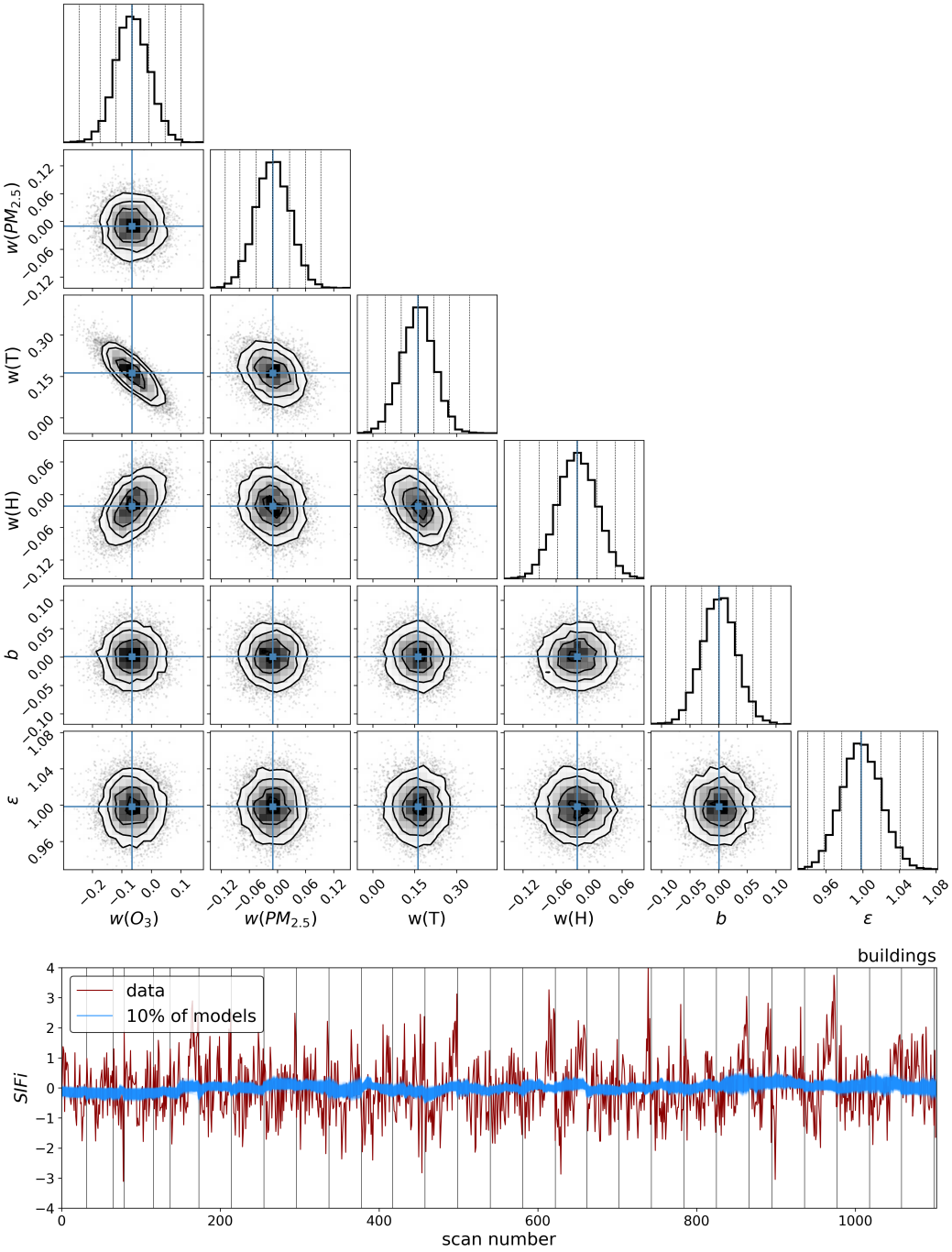

Figure 11. (**Top**): MCMC corner plot of the posterior distribution of air quality parameters for buildings. (**Bottom**): The measured SIF indicator (*SIFi*) values as a function of scan number with 10% of randomly selected models from those identified as probable by MCMC, with the vertical lines indicating the change in days.

Table 3. Top: MCMC median of atmospheric coefficient parameters to model the SIF indicator (*SIFi*) values at full (848-channel) spectral resolution, together with the 3σ uncertainty shown as super- and subscripts, which include the full parameter covariance derived from the 3σ contours in the posteriors provided in Figures 10 and 11. Bottom: Model evaluation statistics for the maximum likelihood solution for vegetation and buildings.

		Vegetation	**Buildings**
parameters	O_3	$0.16^{+0.13}_{-0.13}$	$-0.07^{+0.18}_{-0.17}$ *
	$PM_{2.5}$	$-0.23^{+0.08}_{-0.09}$	$-0.01^{+0.10}_{-0.10}$ *
	Temperature	$0.53^{+0.13}_{-0.14}$	$0.16^{+0.18}_{-0.19}$ ***
	Humidity	$-0.28^{+0.08}_{-0.08}$	$-0.02^{+0.11}_{-0.10}$ *
	b (offset)	$0.00^{+0.07}_{-0.07}$ *	$0.00^{+0.09}_{-0.09}$ *
	ε	$0.78^{+0.05}_{-0.05}$	$1.00^{+0.06}_{-0.07}$
statistics	r^2	0.40	0.01
	Adj. r^2	0.40	0.01
	F-statistic	183.30	3.08
	Prob. (F-stat.)	0.00	0.02
	Log-likelihood	−1281.60	−1557.70

* and *** indicate measurements consistent with zero within 1σ or 3σ uncertainty, respectively.

To show the goodness of fit of models to both vegetation and buildings, Figure 12 shows the measured and predicted values of *SIFi* with the ranges of uncertainties obtained for each scan from the MCMC parameter values, as well as the χ^2 per degree of freedom ($\chi^2/\text{dof} = \sum(f_t - \overrightarrow{P} \cdot \overrightarrow{w})^2/\epsilon^2$, where the sum is over time steps) distribution of all possible models. The distribution of χ^2/dof for both vegetation and buildings centered around 1 indicates that the extent of the match between the predicted and measured values of *SIFi* produces a good fit within the error variance. For a more quantitative description of the goodness of fit of the models to the measured *SIFi* values, we show the resulting statistics for both vegetation and building models in Table 3. The table shows that all air quality parameter coefficients in the model of the *SIFi* of vegetation health are not consistent with zero, while those of the buildings models are all consistent with zero to within 3σ uncertainty. Moreover, 40% of the variation in this linear model of vegetation health is explained by the air quality model, while only 1% of variation is explained in buildings.

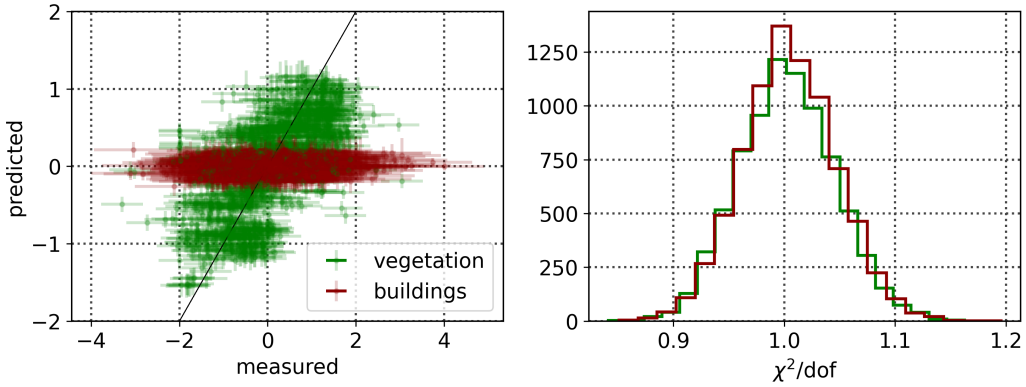

Figure 12. Measured vs. predicted SIF indicator (*SIFi*) values (**left**), and χ^2 per degree of freedom (**right**) for vegetation and buildings models.

3.2. Principal Component Analysis (PCA)

As we describe in Section 2.4, the 848-channel Compound Ratios of vegetation and buildings were projected onto the first four PCA components shown in Figures 8 and 9. The

air quality parameter coefficients, their 3σ uncertainties, and the goodness of fit statistics of the maximum likelihood solution for our linear model are summarized in Table 4. The full posterior distributions for fits to each PCA component amplitude (for both vegetation and buildings) are provided in the Supplementary Materials.

The results in Table 4 show that the maximum likelihood solution for the 4th principal component of vegetation, which has an explained variance of 1.4%, produces the highest r^2 value of 47%, while component 1 (EV = 70.5%) produces results most similar to those obtained with the *SIFi*, both in terms of air quality coefficients and r^2 value. The lowest performing principal component of vegetation (component 3) shows an r^2 value of 11%, which is 2.6× that of the best performing building component (component 1, r^2 = 4%). It is worth noting that all the air quality coefficients for principal components 1 and 2 of the buildings are consistent with zero to within 3σ uncertainty, while in component 3 temperature has a non-zero coefficient, and $PM_{2.5}$ and humidity are not consistent with zero for component 4.

The low level of explained variance (r^2 ∼4%) is likely due to a combination of factors, chief of which are the assumptions undertaken when calculating the Compound Ratios outlined in Section 2.2 regarding the constant reflectivity of buildings. Relative to the significant changes in reflectivity observed in the spectra of vegetation, the assumption that the reflectivity of buildings remains constant over time holds true, as seen in Figure 3. However, the PCA components in Figure 9 show that there is a small amount of structure within the noise in the Compound Ratio of buildings. This can be explained by the fact that dirt, moss, and other pollutants as well as water following rainy days can stick to the sides of buildings, which may cause a slight change in their spectra over time. Moreover, the reflectivity of concrete varies depending on a number of factors including porosity, color, water content, and even surface moisture [134,135], which are correlated with changes in humidity and temperature. This effect is evident in the parameter coefficients for PCA components in Table 4, where components 3 and 4 show parameter coefficient values for temperature and humidity, respectively, that are non-zero to within uncertainty. Another potential source of correlation is windows in the buildings that could be reflecting the spectra of the nearby vegetation or the sky, thus producing small change in the Compound Ratio spectrum over time.

Table 4. Top: MCMC median of atmospheric coefficient parameters to model the PC amplitude of each PCA component at full spectral resolution, together with the 3σ uncertainty shown as super- and subscripts, which include the full parameter covariance derived from the 3σ contours in the posteriors provided in Figures S1–S8 in Supplementary Materials. Bottom: Model evaluation statistics for the maximum likelihood solution for vegetation and buildings.

		Component 1		**Component 2**		**Component 3**		**Component 4**	
		Vegetation	**Buildings**	**Vegetation**	**Buildings**	**Vegetation**	**Buildings**	**Vegetation**	**Buildings**
parameters	O_3	$-0.14^{+0.13}_{-0.13}$	$0.09^{+0.16}_{-0.17}$ **	$-0.17^{+0.15}_{-0.16}$	$0.07^{+0.15}_{-0.16}$ **	$-0.15^{+0.16}_{-0.16}$ ***	$-0.06^{+0.15}_{-0.16}$ **	$0.14^{+0.12}_{-0.12}$	$-0.02^{+0.16}_{-0.15}$ *
	$PM_{2.5}$	$0.24^{+0.08}_{-0.09}$	$-0.02^{+0.11}_{-0.11}$ *	$-0.03^{+0.10}_{-0.09}$ *	$-0.08^{+0.10}_{-0.10}$ **	$-0.04^{+0.11}_{-0.10}$ **	$0.00^{+0.11}_{-0.11}$ *	$0.15^{+0.08}_{-0.08}$	$0.11^{+0.10}_{-0.10}$
	Temperature	$-0.46^{+0.14}_{-0.14}$	$0.14^{+0.17}_{-0.16}$ ***	$-0.15^{+0.17}_{-0.16}$ ***	$0.04^{+0.17}_{-0.17}$ *	$0.34^{+0.17}_{-0.17}$	$0.24^{+0.16}_{-0.17}$	$0.19^{+0.13}_{-0.13}$	$-0.05^{+0.17}_{-0.16}$ *
	Humidity	$0.38^{+0.08}_{-0.09}$	$-0.03^{+0.10}_{-0.10}$ *	$-0.15^{+0.10}_{-0.10}$	$-0.09^{+0.11}_{-0.10}$ ***	$0.17^{+0.10}_{-0.10}$	$-0.10^{+0.11}_{-0.11}$ ***	$0.50^{+0.08}_{-0.08}$	$-0.18^{+0.10}_{-0.10}$
	b (offset)	$0.00^{+0.07}_{-0.07}$ *	$0.00^{+0.09}_{-0.09}$ *	$0.00^{+0.09}_{-0.08}$ *	$-0.00^{+0.08}_{-0.09}$ *	$0.00^{+0.09}_{-0.09}$ *	$0.00^{+0.09}_{-0.09}$ *	$0.00^{+0.07}_{-0.06}$ *	$-0.00^{+0.08}_{-0.08}$ *
	ε	$0.79^{+0.04}_{-0.05}$	$0.98^{+0.06}_{-0.07}$	$0.94^{+0.06}_{-0.06}$	$0.99^{+0.06}_{-0.07}$	$0.95^{+0.06}_{-0.06}$	$0.98^{+0.06}_{-0.07}$	$0.73^{+0.05}_{-0.05}$	$0.98^{+0.05}_{-0.07}$
statistics	r^2	0.38	0.04	0.13	0.02	0.11	0.04	0.47	0.04
	Adj. r^2	0.38	0.04	0.13	0.02	0.11	0.03	0.47	0.03
	F-statistic	168.70	11.85	40.85	6.17	33.12	10.62	247.60	10.44
	Prob. (F-stat.)	0.00	0.00	0.00	0.00	0.00	0.00	0.00	0.00
	Log-likelihood	−1299.50	−1540.40	−1487.20	−1551.40	−1500.80	−1542.70	−1209.20	−1543.10

*, **, and *** indicate measurements consistent with zero within 1σ, 2σ, or 3σ uncertainty, respectively.

3.3. Isolating Solar Angles and Diurnal Effects

The methodology in Section 2.2 is designed to isolate the apparent reflectance from the effects of atmospheric attenuation and irradiance. However, as seen in Equation (3), there remains an irradiance term (E) with which the solar-induced fluorescence is normalized, and studies have shown that the direct and diffuse fractions of the sun-sensor geometry affect vegetation reflectance, with an impact on uncertainty ranging from ∼9% up to ∼58% for various vegetation indices and solar-induced fluorescence [83,84]. Furthermore, due to the diurnal change in solar angle, coupled with the diurnal change in temperatures and ozone concentrations, the question arises as to whether the correlations uncovered in the previous sections may solely be the product of the correlation between diurnal changes in solar angles and vegetation health indicators rather than impact of air quality changes on vegetation health.

To address this concern, we isolate the diurnal behavior by dividing our hyperspectral samples into independent time series separated by their acquisition time of day (i.e., the hyperspectral images captured at 08h00 each day form a separate series from those captured at 08h15, etc.). This results in 41 independent series of spectra captured between 08h00 and 18h00 in 15 min intervals, with each time-of-day series being composed of 27 scans on average. Since all scans in each separate series are acquired at the same time of day, any changes in temperature, ozone, or vegetation health indicators including solar-induced fluorescence should be independent of the diurnal changes in solar angles. We note that while solar incidence angle can measurably vary over the course of a month, the data used for this work were acquired during the month of May into early June when the sun is approaching aphelion and the variation in solar declination is at its annual minimum. Given that New York City is at a latitude of 41°N, during the period of this study the solar incidence angle exhibits negligible change across the entire month with variation on the order of 2–3 degrees. The $SIFi$ for each series is standardized across days independently for both vegetation and building pixels as shown in Figure 13 with daily variations at fixed time of day shown horizontally (the time series for each day is shown vertically). Here, it is evident that vegetation $SIFi$ exhibits more structured variation at each time of day and across days than does the building $SIFi$, which is dominated by noise.

As in Section 3.1, MCMC sampling of the likelihood surface is performed for each time-of-day series independently for both vegetation and building *SIFi* correlations with the various air quality parameters. Figure 14 shows the range of r^2 of the linear model fit for each series, where it is evident that a linear model composed of O_3, $PM_{2.5}$, temperature, and humidity is far more capable of explaining the variations in the time-of-day series of vegetation *SIFi*, with a median r^2 of 0.51, than the buildings' with a median r^2 of 0.16. Moreover, considering only the optimal times in the day in terms of lighting between 09h30 and 15h30, the vegetation median r^2 is 0.58, while the buildings' is 0.15. Furthermore, by repeatedly drawing random time-of-day series, each with 27 values drawn from a univariate Gaussian (whose width is set to be equal to the standard deviation of the observed building time-of-day series), and correlating them with the MCMC sampled models, we find that the frequency and magnitude of high-r^2 anomalous correlations are consistent with those seen in the results for buildings. Figure 15 shows the coefficients for O_3, $PM_{2.5}$, temperature, and humidity and their 3σ uncertainty for each of the time-of-day *SIFi* series for vegetation and buildings. While the mean values of the coefficients for vegetation show more structure and are generally not consistent with zero to within 1σ uncertainty relative to the noisier trends seen in the building coefficients, all coefficients for both are generally consistent with zero to within 3σ uncertainty.

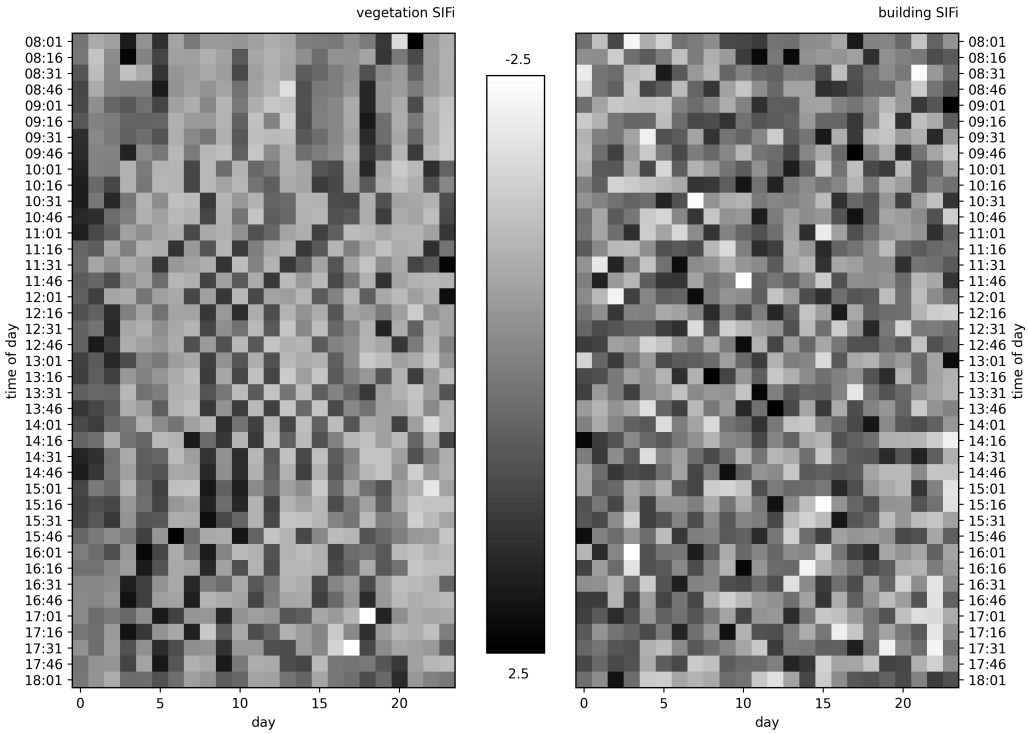

Figure 13. Solar-Induced Fluorescence indicator (*SIFi*) for vegetation (**left**) and buildings (**right**) standardized horizontally for each time-of-day series plotted for each day vertically. Each horizontal time-of-day series is independent of diurnal correlations between solar angles, temperature, ozone, and vegetation health indicators since each data point is captured daily at the same time.

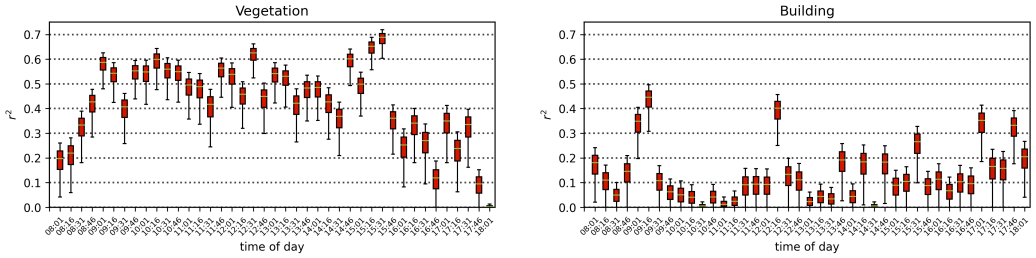

Figure 14. r^2 values that portray the levels at which linear models composed of O_3, $PM_{2.5}$, temperature, and humidity are capable of explaining the variability in each series of standardized time-of-day Solar-Induced Fluorescence indicator (*SIFi*) for vegetation (**left**) and buildings (**right**).

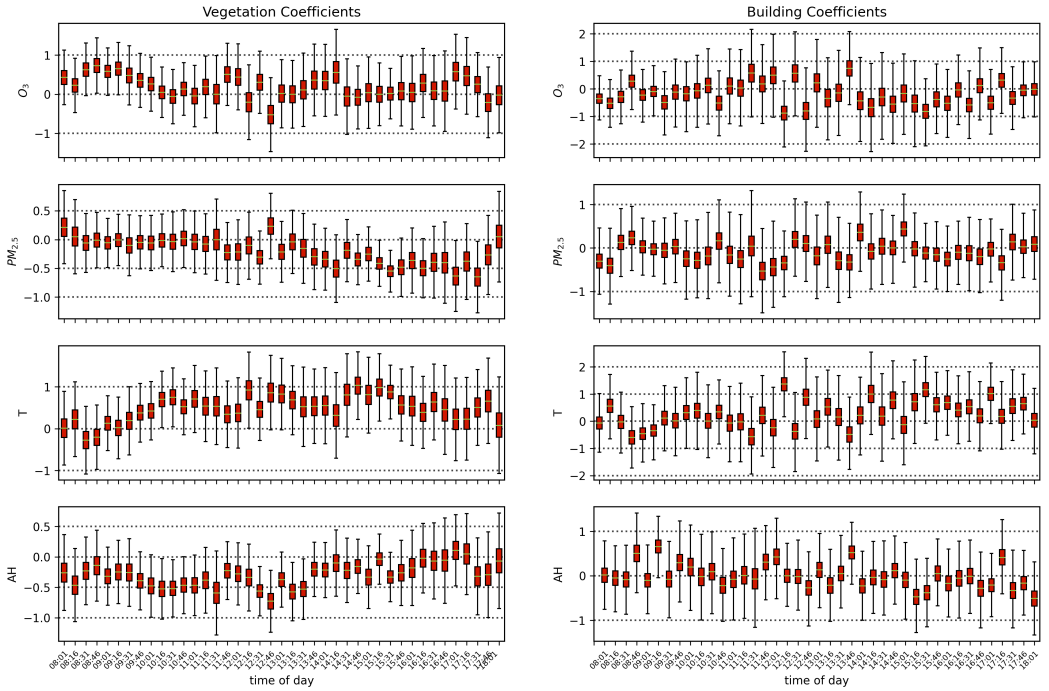

Figure 15. The coefficients for models containing all air quality parameters: O_3, $PM_{2.5}$, temperature, and absolute humidity, for each series of standardized time-of-day Solar-Induced Fluorescence indicator (*SIFi*) for vegetation (**left**) and buildings (**right**).

It is also worth noting that in Figure 15, the coefficient values for O_3 and temperature exhibit a significantly strong anti-correlation. To test the possibility that the cause of the coefficients for ozone and temperature being consistent with zero to within 3σ uncertainty may be in part due to this covariance, the MCMC sampling was repeated with temperature and humidity eliminated from the linear model, leaving only O_3 and $PM_{2.5}$. The resulting models have a median r^2 of 0.38 for vegetation (0.42 if only 09h30 to 15h30 times are included), while those of the buildings have a median r^2 of 0.04. The resulting coefficients for O_3 and $PM_{2.5}$ for all sampled models of each time-of-day series are shown in Figure 16. While O_3 and $PM_{2.5}$ coefficients (median values of 0.05 and -0.03, respectively) are consistent with zero within 3σ uncertainty for the buildings, for vegetation the coefficients of O_3 have a median of 0.66 and are not consistent with zero within 3σ uncertainty and the coefficients of $PM_{2.5}$ have a median of -0.22 and are not consistent with zero within $1-2\sigma$ uncertainty in general.

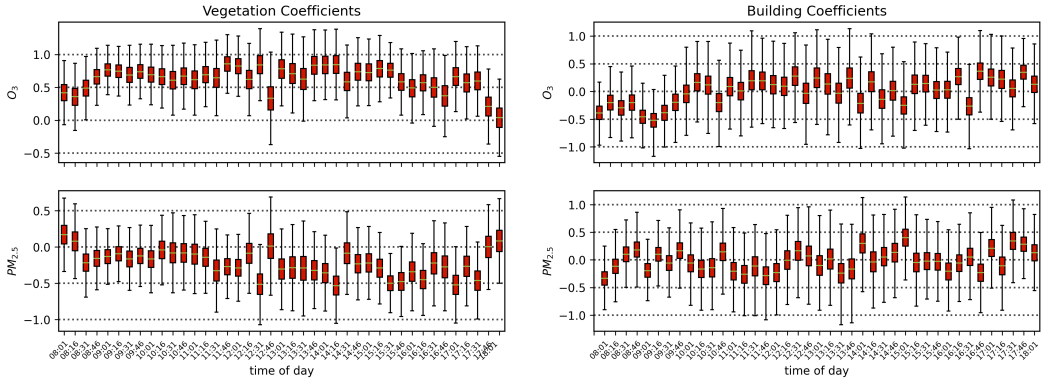

Figure 16. The coefficients for models that only contain O_3 and $PM_{2.5}$ concentrations, with temperature and absolute humidity absent, for each series of standardized time-of-day Solar-Induced Fluorescence indicator (*SIFi*) for vegetation (**left**) and buildings (**right**).

3.4. Temperature and Ozone

Strong correlations between O_3 concentrations and temperature are clearly visible in the scatter plots in Figure 17, as well as both exhibiting a measurable impact on the *SIFi* value of vegetation. Even though both variables are correlated through the diurnal cycle, the results in Section 3.3 show that when time of day is isolated, the impact of ozone on the *SIFi* is suppressed when temperature is included as a variable in the linear model in comparison with its effect when temperature is removed. It can then be inferred that the identified impact of ozone and temperature on the measured health of vegetation in this work thus far is intertwined, thus producing the question of whether the impact of ozone is a transitive correlation that is purely the result of the impact of temperature change on varying photosynthetic rates, or whether ozone is truly impacting vegetation health.

To address this question and identify the impact of O_3 on the measured change in vegetation health, we separate all scans into individual series based on their temperature and standardize their O_3 concentrations, and vegetation and building *SIFi* values. Discarding series with fewer than 10 scans leaves 38 different series with a maximum of 56 and an average of 25 data points ranging in temperature from 9.5 °C to 31 °C. Figure 18 shows the trends in standardized O_3 and vegetation and building *SIFi* values for each individual temperature together with their associated Pearson's correlation coefficient values. On average, vegetation *SIFi* has $r = 0.31$ with ozone, while buildings have $r = -0.05$. This indicates that, independent of temperature, the effect of ozone on vegetation health remains significant.

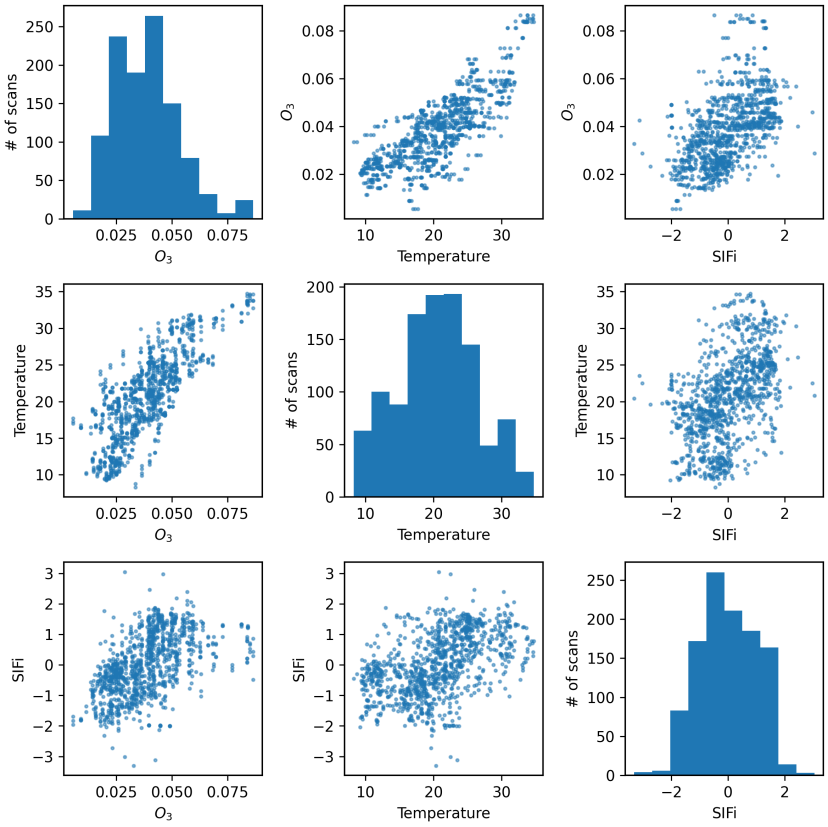

Figure 17. Scatter matrix showing the distribution of O_3 concentrations (in g/cm^3), temperature (in °C), and *SIFi* and their correlations.

It is worth mentioning that controlling for temperature also provides control for temperature-dependent processes that might affect the correlation between O_3 concentrations and vegetation health. For example, isoprene (C_5H_8) is an abundant biogenic volatile organic compound, primarily emitted by plants, that is highly reactive and considered an important precursor for surface ozone formation [136]. Additionally, isoprene emissions by plants reach a maximum in summer between midday and afternoon that coincide with higher levels of sunshine and ambient temperatures [137], which are similar conditions required for increased levels of photosynthesis. Furthermore, isoprene production in plants is used as a heat-tolerance mechanism that increases in higher temperatures, thus resulting in the production of more O_3 [138]. However, finding a correlation between *SIFi* and O_3 while controlling for temperature leads to the conclusion that it is unlikely that isoprene production is the main driver of the observed correlation.

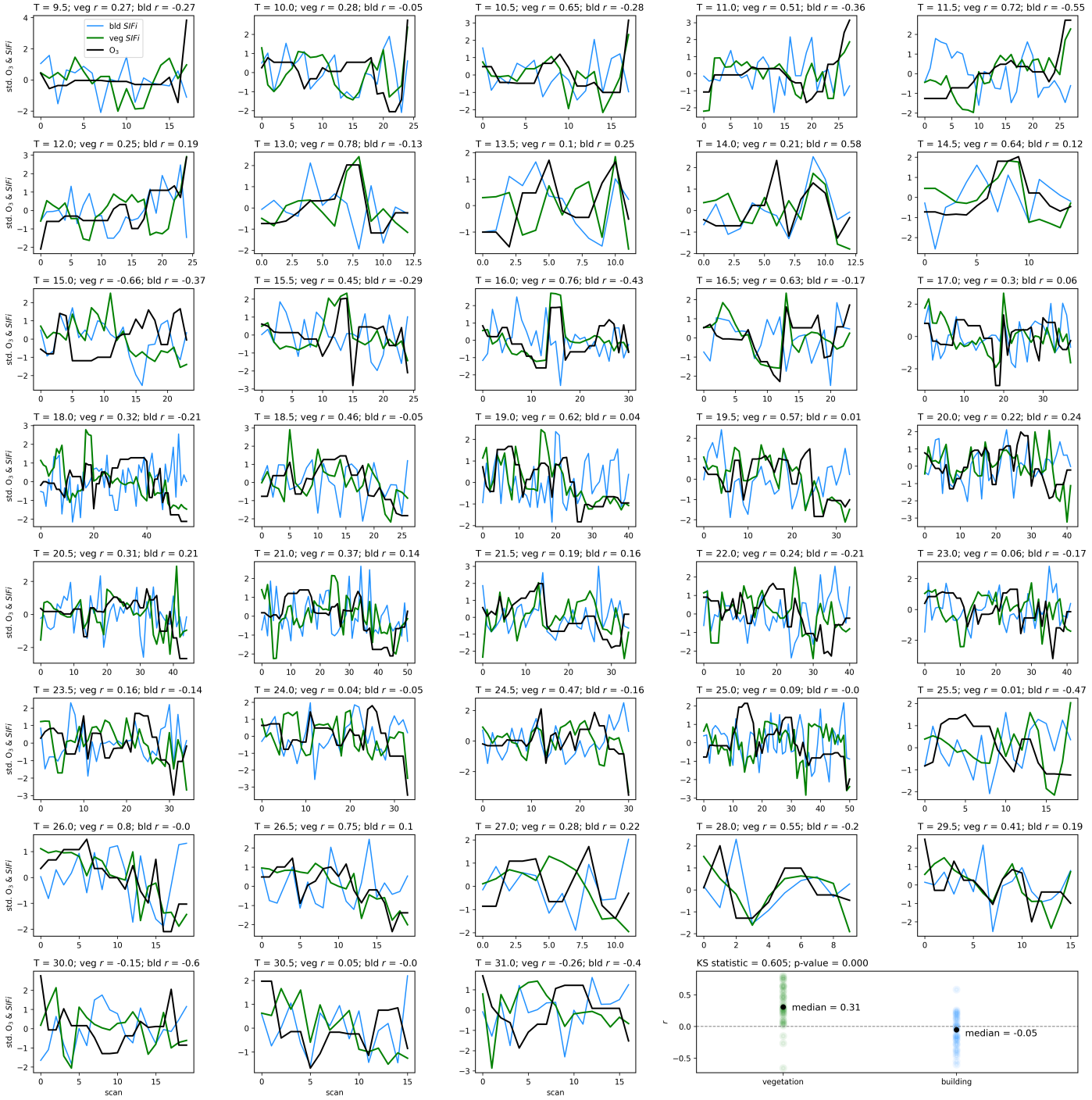

Figure 18. Each plot shows the trends in standardized O_3 concentrations (black), *SIFi* for vegetation (green), and *SIFi* for the buildings (blue) for scans of equal temperature. A summary of the Pearson's correlation coefficients of these time series for both the vegetation and buildings are shown in the figure in the bottom right corner, and indicates a clear correlation between ozone and vegetation health (but not between ozone and building pixels) when temperature is held constant.

4. Discussion

The results in the previous sections show that, regardless of the indicator used to quantify vegetation health, following our proposed method for atmospheric correction, there is a far stronger correlation between time-dependent changes in air quality and vegetation health than with that same indicator applied to nearby building spectra. Using the simple ratio of Compound Ratios at 0.75 µm to 0.9 µm to indicate the change in

Solar-Induced Fluorescence (SIF), 40% of variation in the SIF indicator (*SIFi*) with time is explained using the simple linear model of air quality parameters (O_3, $PM_{2.5}$, temperature, and humidity). On the other hand, <2% of the variation is explained in the *SIFi* values of buildings. Given that the *SIFi* changes provide cues concerning the health of vegetation, particularly the chlorophyll AB content and photosynthetic rates, it can be inferred from this result that the high explained variance of air quality parameters with *SIFi* changes is an indication that air quality is producing a measurable impact on the health of vegetation. Furthermore, all air quality parameter coefficients in the linear model of the *SIFi* for buildings are consistent with zero to within 3σ uncertainty (fully covariant uncertainties derived from MCMC sampling of the likelihood), while none are consistent with zero for vegetation.

Similar results were obtained using Principal Component Analysis (PCA), where the variations in the amplitude of each of the four Principal Components (PCs) with time were used in the modeling. Component 1 showed an r^2 of 38% for vegetation and 4% for buildings and, while components 2 and 3 showed lower correlation with changes in air quality than components 1 and 4, their correlations were still larger than those between building PCA amplitudes and air quality. Even though component 4 shows the least Explained Variance (EV) of 1.4%, it exhibited the strongest correlation of 47% for vegetation and only 4% for buildings. Interpreting this result is challenging since PCA produces components that are orthogonal by design and so explicating their structure as being representative of a physical property is not feasible. However, qualitatively assessing the shape of component 4 in Figure 8 reveals characteristic structures such as an inverted green peak, red edge, and SIF peaks that are particularly effective at indicating vegetation health. The fact that the principal component with the least explained variance shows these features together with the greatest correlation with changes in air quality is an indication that much of the spectrum of vegetation does not contain important information regarding its health. At high spectral resolutions, it is inevitable that redundant information will be present, as well as temporal variation that is not related to vegetation health. Therefore, the practice of using the ratio of particular wavelengths, as is the case with the *SIFi*, or dimensionality reduction processes such as PCA lends itself to extracting the essential information needed to infer vegetation health.

MCMC results showed a positive correlation for changes in ozone and temperature with changes in *SIFi* values, and a negative correlation for variation in $PM_{2.5}$ and humidity. This result is also seen with NDVI in Appendix A.1, and the opposite is seen in component 1 of PCA (noting that the amplitude of this component resembles the mean spectrum of vegetation reflected about the x-axis). Given the functional connection between photosynthesis and *SIFi*, and the negative effects of $PM_{2.5}$ on photosynthetic rate, the obtained negative correlation is expected. Humidity is known to increase with increased opaque cloud cover [139], which results in reduced sunshine and can therefore explain the resulting negative correlation with photosynthetic rate. Ozone, on the other hand, shows a counter-intuitive correlation given the known adverse effects it has on photosynthesis. The prevalent consensus in the literature over the past two decades suggests that increased surface ozone results in a decrease in chlorophyll content, causing adverse effects on tree biomass and visible leaf injury, leading to decreased photosynthesis [21–24]. However, studies demonstrating these effects are traditionally carried out under controlled environmental conditions using plant chambers to expose plants to known O_3 concentrations. While values vary by species, O_3 levels of 200–300 ppb are required for the impact on plant physiology to be measurable [28]. Ozone levels in excess of 100 ppb are relatively rare in New York City, our data peak at ∼80 ppb (see Figure 5). Since O_3 does not accumulate in plant tissue and given the difficulty in separating its impacts from those of other environmental variables, conclusive proof of its impact on urban vegetation is lacking in the literature, and our results do not contradict previous findings. The positive correlation of ozone concentration with *SIFi* values found in this work can potentially be explained by several environmental correlations and dependencies that cause this observed result. One such explanation is the

co-occurrence of ozone with carbon dioxide. Since the Industrial Revolution, the concentrations of atmospheric carbon dioxide and ozone have increased in tandem [140]. CO_2 generally enhances vegetation productivity and growth, and given the co-occurrence of O_3 and CO_2, the positive correlation obtained in this work between variations in vegetation health indicators and O_3 may be the result of increased CO_2 concentrations.

Air quality parameters, particularly O_3 concentrations and temperatures, are known to exhibit a diurnal behavior that is correlated with solar angle. Solar-induced fluorescence is also known to vary with sun-sensor geometry, and with a fixed sensor view, the variation in solar zenith angle can result in a diurnal pattern in SIF that resembles the diurnal change in temperature, which also affects O_3 concentrations. By separating the obtained scans into independent time series by the time of day of their acquisition, we isolate the impact of air quality from that of the diurnal cycle and observe that with a linear model of air quality parameters fit to each time-of-day series separately, the vegetation exhibits a median r^2 of 0.51, while the buildings show a far lower median value of 0.16. Furthermore, by isolating the scans into independent series based on their temperature, we find that vegetation on average has a Pearson's correlation coefficient value of 0.31 with ozone, while the buildings' is -0.05. These results show that while perhaps some correlation of air quality with vegetation health may be influenced by diurnal changes in solar angle and temperature, it is clear that the impact of O_3 on vegetation health remains significant when controlling for solar angle and temperature.

In all test cases, the amount of variation explained by models fitting a linear combination of air quality parameters to the change in quantified measures of the spectra of vegetation was higher than that for buildings, however, it did not exceed 50%. The relatively low r^2 in the vegetation models may be due to a variety of factors. While we expect that the effect is small given the unique spectrum of vegetation, one such factor is the accuracy of *k*-means clustering, whereby non-vegetation pixels can potentially be mislabeled as vegetation. The inclusion of misidentified pixels could reduce the correlation with air quality if, for example, built structures are mislabeled as vegetation since (as we have found for building spectra) the correlation with air quality is weaker for built structures than vegetation. However, a likely more important consideration is that in this work we assume a simple linear combination of air quality parameters. Given the complexity in the interactions between air quality and vegetation, the results could potentially be improved using a more complex model. Finally, another important consideration potentially affecting the goodness of fit of the model is the fact that vegetation health is dependent on a complex variety and combination of factors besides the air quality parameters selected in this work. Vegetation health is also dependent on soil quality [141], water runoff and retention [142], direct sunlight and shade [143], pests, disease, invasive species and weeds [58,61], and a plethora of other factors that are outside the scope of this work. Nonetheless, we argue that the r^2 values for the linear air quality models and vegetation health found here are sufficient to indicate a robust correlation, especially in comparison with those obtained for the buildings.

5. Conclusions

Using a Visible and Near-Infrared (VNIR) single slit, scanning spectrograph, deployed by the Urban Observatory (UO) [71–74] in New York City, that captures 848 spectral channels in the 0.4–1.0 μm wavelength range, we obtained side-facing scans of an urban scene in 15 min intervals between 08h00 and 18h00 for 30 days between 3 May and 6 June 2016. Selecting vegetation pixels using unsupervised *k*-means clustering, together with nearby building pixels split into two random sets (sets *a* and *b*) as controls, we present the use of the *Compound Ratio* to remove the contribution of solar irradiance and atmospheric attenuation from the change in apparent reflectance in the mean spectra over time. We then correlated vegetation health indicators from the Compound Ratio of vegetation and buildings with publicly available concentrations of ozone (O_3) and particulate matter ($PM_{2.5}$), temperature, and humidity temporally coincident with the VNIR scans. For the

vegetation health indicators, we used both a two-channel Solar-Induced Fluorescence (SIF) ratio of 0.75 µm to 0.9 µm ($SIFi$) as well as amplitudes of a Principal Component Analysis (PCA) decomposition designed to capture broader spectral features.

Modeling these vegetation health indicators as a simple linear combination of the air quality and environmental parameters, and using Markov Chain Monte Carlo (MCMC) sampling of the likelihood to generate posterior distributions and determine parameter covariances, we found a strong correlation between changes in air quality parameters and variations in both indicators for vegetation health. Variations in $SIFi$ values show significantly stronger correlation with air quality parameters for vegetation ($r^2 = 0.40$) compared to our control sample of buildings ($r^2 = 0.01$), and all air quality parameter coefficients for the building model were consistent with zero to within 3σ uncertainty. Similar results were obtained for PC amplitudes, with the strongest correlation between air quality parameters and variations in vegetation health measures found with the fourth PCA component ($r^2 = 0.47$). By isolating the impact of the diurnal sun-sensor geometry on changes in solar-induced fluorescence, we show that the influence of air quality on vegetation health remains significant ($\tilde{r}^2 = 0.51$) in comparison with that of the buildings ($\tilde{r}^2 = 0.16$). Furthermore, separating into series of constant temperature, we find that the impact of O_3 on vegetation health is measurably independent of the correlations between diurnal sun-sensor geometry, solar-induced fluorescence, and temperature.

The strong correlation between a simple linear combination of air quality parameters and variations in all vegetation health indicators, especially the PCA decomposition results that encode information from the full resolution spectra, demonstrates the potential of reversing the analysis and using urban vegetation as a bioindicator for air quality. Specifically, the results indicate that it may be possible to extract the air quality parameters from the atmospherically corrected Compound Ratio spectra of urban vegetation by leveraging the ability of statistical models to learn coherent associations between the various spectral channels and their relation with air quality parameters. Evaluating the efficacy of such models to extract air quality from Compound Ratio spectra of vegetation as a function of spectral resolution will be the subject of future work.

Supplementary Materials: The following are available online at https://www.mdpi.com/article/10.3390/rs14163854/s1, Figures S1–S8: MCMC corner plots of posterior distributions for PCA components 1 through 4 of both the vegetation and the buildings.

Author Contributions: Conceptualization, F.Q. and G.D.; methodology, F.Q. and G.D.; software, F.Q., M.S.S. and G.D.; validation, F.Q., M.S.S. and G.D.; formal analysis, F.Q.; investigation, F.Q.; resources, G.D.; data curation, M.S.S. and G.D.; writing—original draft preparation, F.Q.; writing—review and editing, F.Q. and G.D.; visualization, F.Q.; supervision, G.D.; project administration, G.D.; funding acquisition, G.D. All authors have read and agreed to the published version of the manuscript.

Funding: This research was funded by a James S. McDonnell Foundation Complex Systems Scholar Award, grant number 220020434.

Data Availability Statement: Publicly available datasets were analyzed in this study. This data can be found here: http://MUONetwork.org, accessed on 14 June 2022).

Acknowledgments: We thank Steve Koonin for valuable conversations and insights motivating this work. We also thank Gard Groth and Middleton Spectral Vision for their assistance deploying the VNIR camera and data collection.

Conflicts of Interest: The authors declare no conflict of interest.

Appendix A. Air Quality Correlation with Changes in NDVI and PRI

Appendix A.1. Normalized Difference Vegetation Index (NDVI)

The Normalized Difference Vegetation Index (NDVI) is one of the most commonly used vegetation indices in studies of vegetation health, first used in 1974 [144]. The basis for the NDVI is measuring leaf chlorophyll content using the amplitude of the highest light reflectance in the near-infrared relative to the absorption in the red band. The formula

for calculating the NDVI we employ for this work using the Compound Ratio $C_{\lambda,t}$ at wavelength λ and time t is:

$$NDVI_t = \frac{C_{NIR,t} - C_{Red,t}}{C_{NIR,t} + C_{Red,t}} \tag{A1}$$

where we use NIR = 0.75 µm and Red = 0.69 µm as recommended by [145].

Following the calculation of the NDVI for each scan, we apply MCMC modeling as described in Section 2.4 and obtain the full posterior distribution of air quality parameters for both vegetation, as seen in Figure A1, and buildings, in Figure A2. The resulting range of atmospheric parameter coefficients is shown in Table A1 together with the goodness of fit statistics from performing an ordinary least squares fit.

Table A1. Top: MCMC median and 3σ uncertainty (including the full parameter covariance, derived from the MCMC posteriors of atmospheric coefficient parameters to model the NDVI values. Bottom: Model evaluation statistics for the maximum likelihood solution for vegetation and buildings.

		Vegetation	**Buildings**
parameters	O_3	$0.16^{+0.14}_{-0.14}$	$-0.16^{+0.16}_{-0.17}$ ***
	$PM_{2.5}$	$-0.15^{+0.09}_{-0.09}$	$0.03^{+0.10}_{-0.10}$ *
	Temperature	$0.45^{+0.15}_{-0.15}$	$0.02^{+0.17}_{-0.18}$ *
	Humidity	$-0.17^{+0.08}_{-0.10}$	$0.02^{+0.10}_{-0.12}$ *
	b (offset)	$0.00^{+0.07}_{-0.08}$ *	$0.00^{+0.09}_{-0.09}$ *
	ε	$0.84^{+0.05}_{-0.06}$	$0.99^{+0.05}_{-0.07}$
statistics	r^2	0.29	0.02
	Adj. r^2	0.29	0.02
	F-statistic	113.20	5.39
	Prob. (F-stat.)	0.00	0.00
	Log-likelihood	−1373.30	−1553.00

* and *** indicate measurements consistent with zero within 1σ or 3σ uncertainty, respectively.

Consistent with the results obtained using SIF, r^2 using the NDVI for vegetation is significantly higher than for buildings, and all air quality coefficient parameters for the building model are consistent with zero to within uncertainty but not for vegetation. However, the r^2 obtained using the NDVI for vegetation (30%) is slightly lower than that obtained using SIF (40%) and component 4 of PCA (47%).

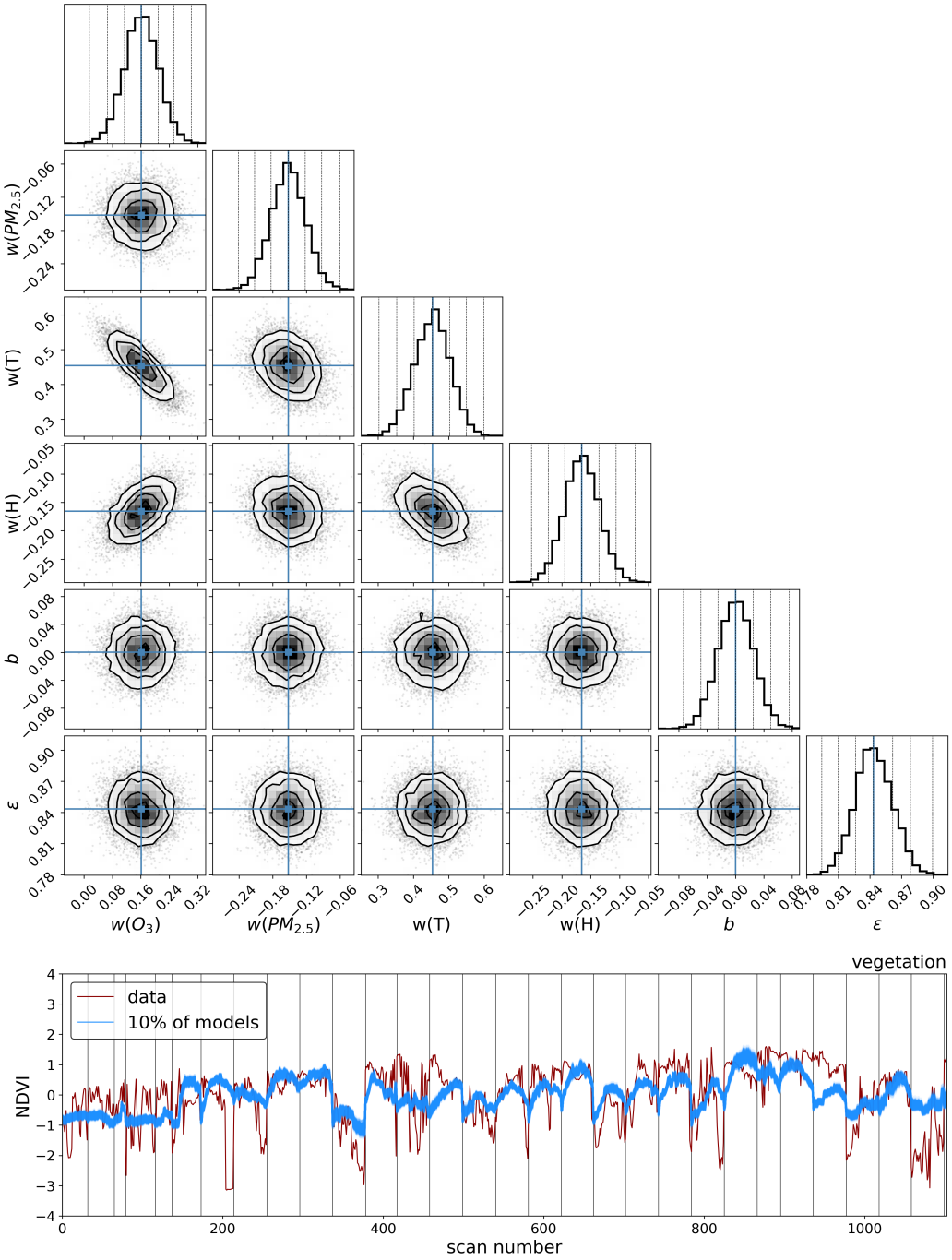

Figure A1. MCMC corner plot of posterior distribution for NDVI of vegetation.

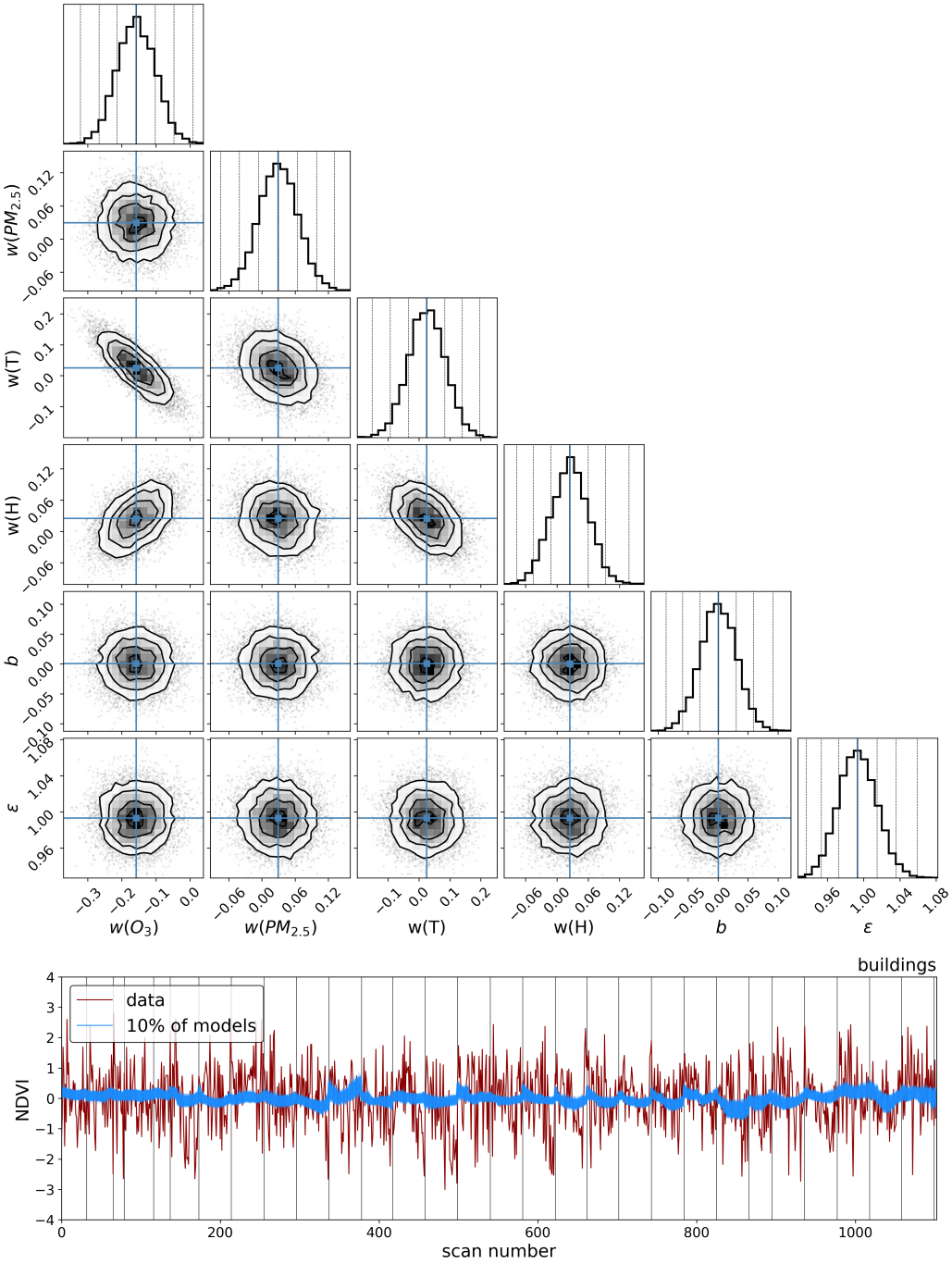

Figure A2. MCMC corner plot of posterior distribution for NDVI of the buildings.

Appendix A.2. Photochemical Reflectance Index (PRI)

Another vegetation index commonly used to assess plant physiology is the Photochemical Reflectance Index (PRI) [63]. It is sensitive to changes in carotenoid pigments, such as xanthophyll, in plant foliage, and functions as a measure of the efficiency of photosynthesis. It is similar in formulation to the NDVI except it focuses on the green peak rather than the red edge in the spectra of vegetation. The formula for calculating the PRI we employ for this work using the Compound Ratio $C_{\lambda,t}$ at wavelength λ and time t is:

$$PRI_t = \frac{C_{0.531,t} - C_{0.57,t}}{C_{0.531,t} + C_{0.57,t}}. \quad \text{(A2)}$$

Following the calculation of the PRI for each scan, we apply MCMC modeling as described in Section 2.4 and obtain the full posterior distribution of air quality parameters for both vegetation, as seen in Figure A3, and buildings, in Figure A4. The resulting range of atmospheric parameter coefficients is shown in Table A2 together with the goodness of fit statistics from performing an ordinary least squares fit.

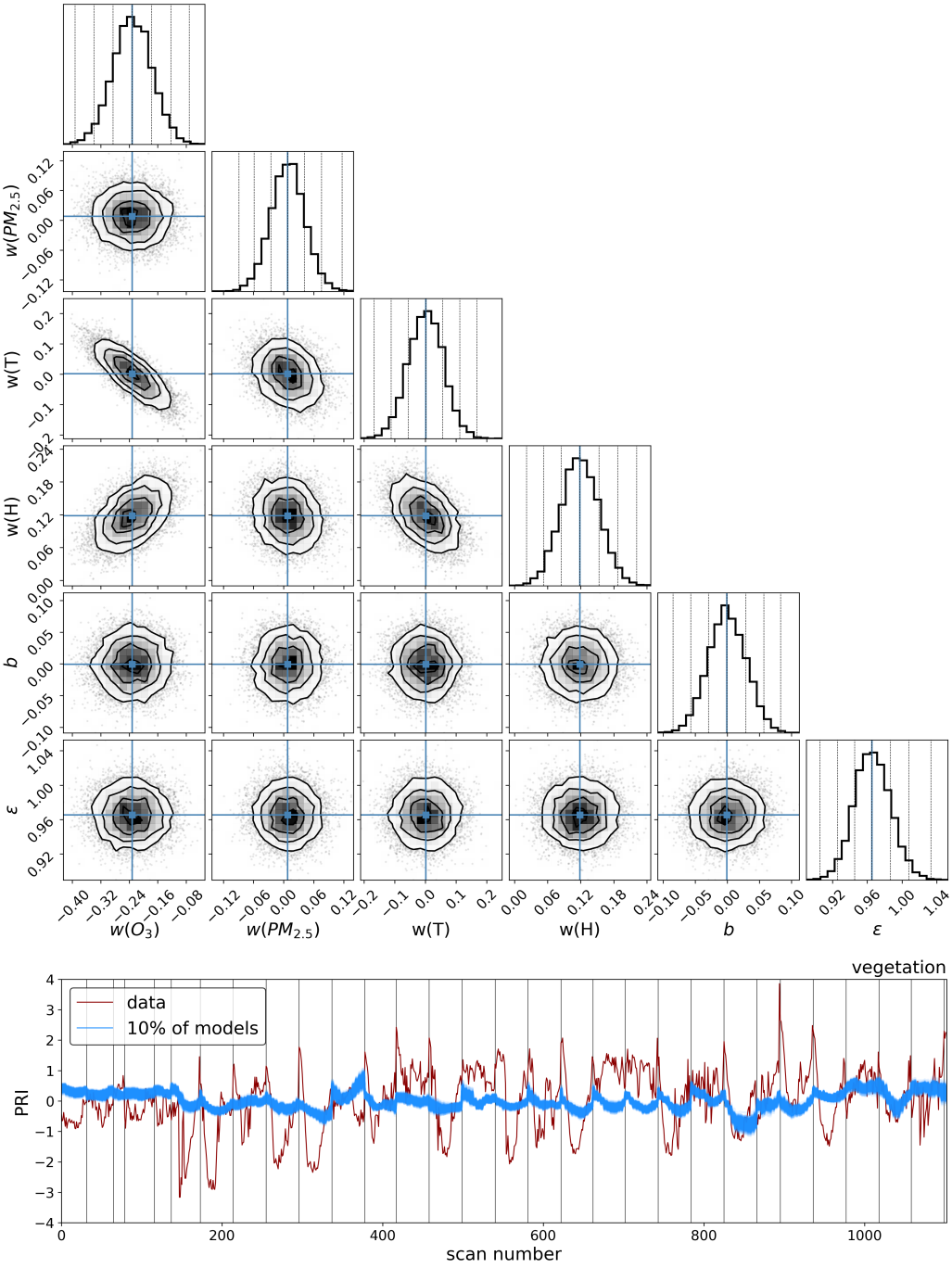

Figure A3. MCMC corner plot of posterior distribution for PRI of vegetation.

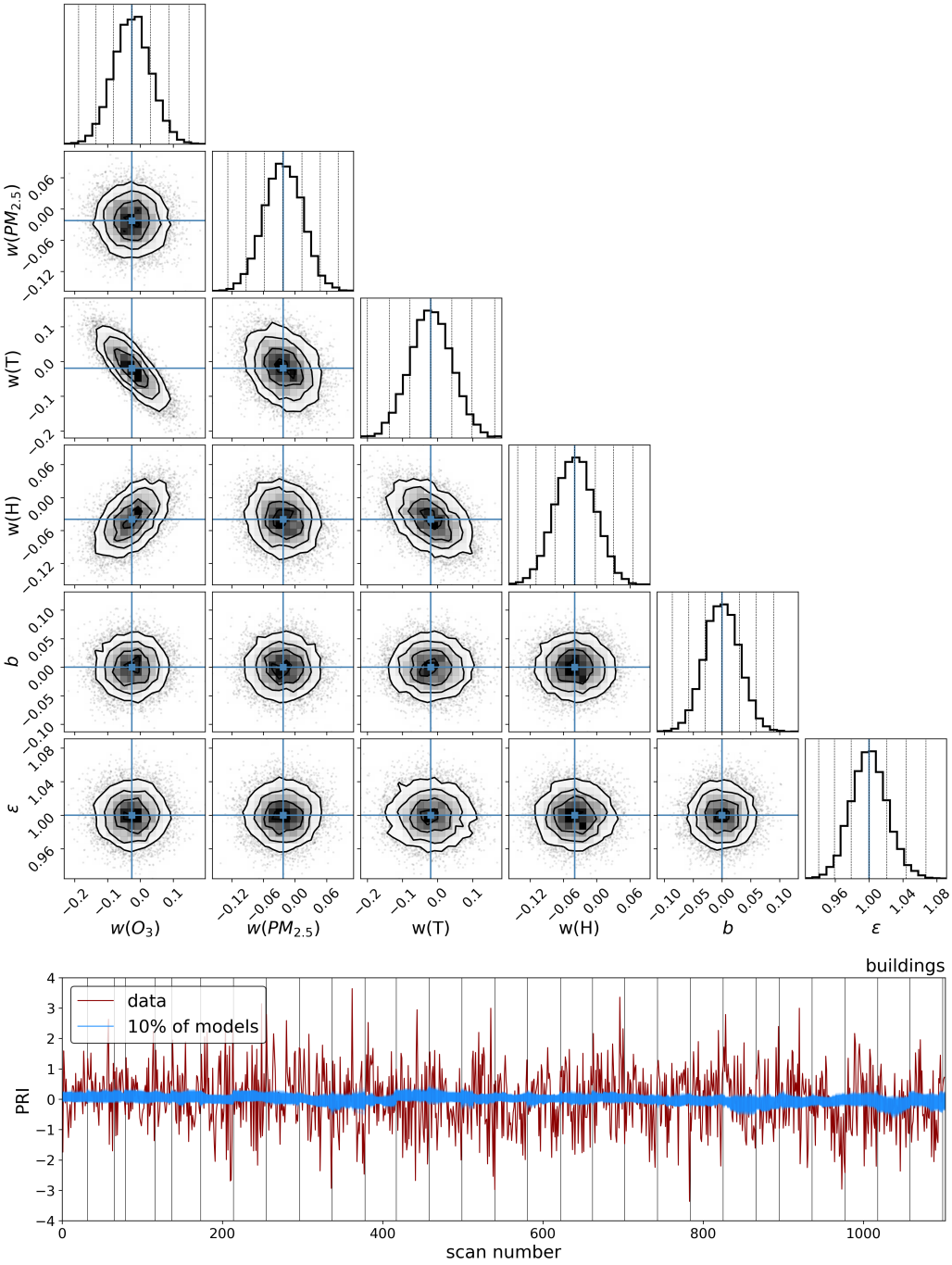

Figure A4. MCMC corner plot of posterior distribution for PRI of the buildings.

Table A2. Top: MCMC median and 3σ uncertainty (including the full parameter covariance, derived from the MCMC posteriors of atmospheric coefficient parameters to model the PRI values. Bottom: Model evaluation statistics for the maximum likelihood solution for vegetation and buildings.

		Vegetation	**Buildings**
parameters	O_3	$-0.33^{+0.15}_{-0.16}$	$-0.01^{+0.17}_{-0.16}$ *
	$PM_{2.5}$	$0.03^{+0.10}_{-0.10}$ *	$-0.02^{+0.11}_{-0.10}$ *
	Temperature	$0.09^{+0.16}_{-0.16}$ **	$-0.05^{+0.17}_{-0.16}$ *
	Humidity	$-0.01^{+0.11}_{-0.12}$ *	$-0.03^{+0.12}_{-0.13}$ *
	b (offset)	$0.00^{+0.08}_{-0.09}$ *	$0.00^{+0.09}_{-0.09}$ *
	ε	$0.97^{+0.06}_{-0.07}$	$1.00^{+0.06}_{-0.07}$
statistics	r^2	0.06	0.01
	Adj. r^2	0.06	0.00
	F-statistic	18.53	1.28
	Prob. (F-stat.)	0.00	0.28
	Log-likelihood	−1527.70	−1561.10

* and ** indicate measurements consistent with zero within 1σ or 2σ uncertainty, respectively.

Although the results show that r^2 for vegetation is greater than that of buildings, which mimics the results obtained from all other vegetation health indicators used in this work, the values of r^2 for both vegetation and buildings are the lowest of any measure by a significant amount. Furthermore, all air quality parameter coefficients of buildings are consistent with zero to within 1σ, and aside from ozone, so are the parameter coefficients for vegetation.

Appendix B. Evaluating Building as Reference

One consideration regarding the methodology described in Section 2.2 that uses the nearby building facade as a control for the Compound Ratio is the extent to which the vegetation area under study is spatially collocated with that building. It is important to ensure that the observed variations are not due to atmospheric variability along the line-of-sight separation between the vegetation and building pixels. As can be seen in Figure 1, the vegetation lies in the foreground of the buildings at a distance of approximately 0.1 km. To investigate the soundness of using the building as atmospheric irradiance and transmission control for the vegetation, we also generate the Compound Ratio time series for other buildings in the scene at distances comparable to or larger than the separation between the vegetation and control building in this work. If the variations found in the vegetation pixels in Section 3 were due to atmospheric variation along the line of sight between the vegetation and control building, we would expect to see variations of similar amplitude and with similar correlation to the air quality variations when comparing our control building to other buildings in the scene. On the other hand, if the variation in vegetation pixels is due exclusively to the effects of air quality on vegetation and not on line-of-sight atmospheric variation between the vegetation and control, we would expect the comparison between that control and other buildings in the scene to have minimal temporal variation and correlation with air quality.

As shown in Figure A5, aside from the building used as control in this work (B), we also look at building r, which is in the same complex as B at a distance of 0.05 km west of the control. We also investigate building y that is at a distance of 0.35 km south-west, building p at a distance of 0.8 km south, and a building closer to the sensor, w, at a distance of 0.3 km north of the control building. Given that these building facades contain a smaller number of pixels than B, we also select a subset of pixels, b, from the control building that contains a similar sample size to the smallest set.

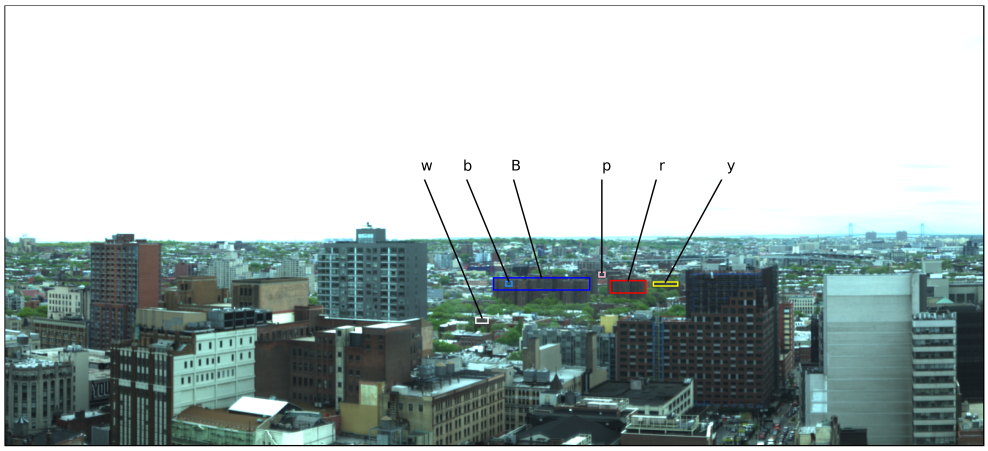

Figure A5. Full-resolution RGB representation of the scene as captured by the Urban Observatory's hyperspectral imaging system. The blue box labeled B shows the buildings used as control throughout this work, which are 0.1 km to the south of the center of the vegetation whose spectra are used in this study. The red box r shows a set of pixels in a building adjacent to the control buildings B at a distance of 0.05 km west. Box p shows a set of pixels belonging to a building 0.8 km south of the control. Box w is closer to the sensor than B, and is 0.3 km north of the control. Box y is a building that is 0.35 km south-west of the control. Box b shows a subset of the control building B with a similar sample size as p.

Treating the various building sets as objects in the same manner as the treatment of the vegetation, the Compound Ratio time series of each set of building pixels was calculated with B as control as per Equation (8). The *SIFi* was similarly calculated using Equation (9) (ratio of Compound Ratios at 0.75 and 0.9 µm) for each building at every scan time. Unlike the treatment seen throughout this work, the time series were not standardized in order to show the difference in amplitude between the *SIFi* of vegetation and those of the buildings. This action does not have an impact on the calculation of the r^2 of the models. The modeling of the time series followed the description provided in Section 2.4.3. Figure A6 shows the measured *SIFi* of the vegetation, control building, and each of the buildings selected in Figure A5 together with a 10% sample of the possible models using the parameters' coefficients produced by MCMC for each object. Table A3 provides the r^2 values for the best-fit model in each object, together with the median values and 3σ range of uncertainties for the atmospheric parameter coefficients.

As can be seen in Figure A6, the signal amplitude of *SIFi* for vegetation is significantly higher than for all the buildings. This includes the building 8× as far from the control building as the vegetation, and shows that the measured changes in the vegetation spectra are far more likely to be due to variations in the properties of vegetation than solely due to any potential atmospheric transmittance. Furthermore, a linear model composed of atmospheric parameters is capable of explaining 44% of the variation in the *SIFi* of vegetation over time, which is 4× higher than that of a building located at 8× the distance to the control building as the vegetation. These results indicate that even if one were to assume that the Compound Ratio of vegetation contains a significant amount of atmospheric transmission artifacts, such artifacts, given the treatment presented in this work, would be incapable of explaining the large amount of variance seen in the vegetation's *SIFi*. As seen in the plots in Figure A6, the linear models of atmospheric parameters track changes in the vegetation's *SIFi* over time to a good degree, but are essentially flat and incapable of tracking the changes in any of the buildings' time series. Moreover, the subset of pixels from the control building, b, which contains only 2% of the sample size of the control building, equal to the sample size of building p, shows a far greater r^2 value (0.11) than the control (0.01) despite being at the same distance. This indicates that much of the variation seen in the buildings' *SIFi* is primarily composed of noise rather than variations due to

uncorrected atmospheric transmittance. All these results provide a clear indication that the measured variations in the vegetation throughout this work are dominated by variations in the health of vegetation, and that any atmospheric transmittance that may have not been corrected with the provided treatment does not have a significant impact on the analysis of the correlation of varying air quality and vegetation health as presented throughout this work.

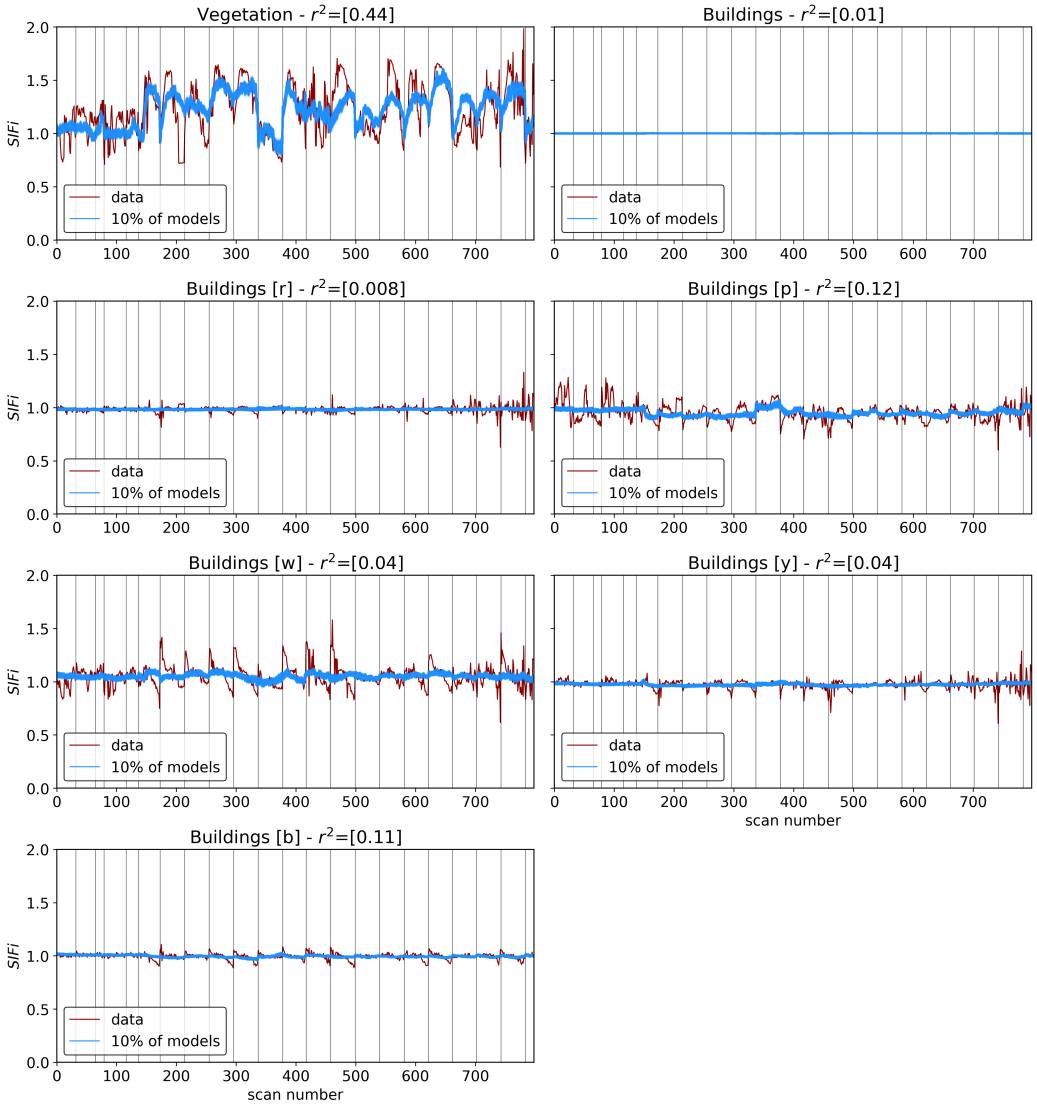

Figure A6. The *SIFi* of vegetation and all objects identified in Figure A5 together with 10% of models randomly selected from those identified as probable by MCMC, with the vertical lines indicating the change in days, and the r^2 of the line of best fit printed in the title of each plot.

Table A3. MCMC results of the various objects selected in Figure A5, including the r^2 values of the line of best fit and the MCMC median and 3σ uncertainty of atmospheric coefficient parameters to model the *SIFi*.

Object	Distance to Control (B)	r^2	O_3	$PM_{2.5}$	Temperature	Humidity	*b* (Offset)	ε
V	0.1 km	0.44	$0.04^{+0.03}_{-0.04}$	$-0.07^{+0.02}_{-0.03}$	$0.15^{+0.04}_{-0.04}$	$-0.05^{+0.03}_{-0.03}$	$1.25^{+0.03}_{-0.03}$	$0.18^{+0.01}_{-0.01}$
B	0 km	0.01	$-0.0002^{+0.0007}_{-0.0007}$ *	$0.0002^{+0.0004}_{-0.0004}$ *	$0.0002^{+0.0007}_{-0.0007}$ *	$-0.0004^{+0.0005}_{-0.0005}$ ***	$1.0007^{+0.0004}_{-0.0004}$	$0.0029^{+0.0002}_{-0.0002}$
r	0.05 km	0.01	$-0.002^{+0.009}_{-0.008}$ *	$0.001^{+0.005}_{-0.005}$ *	$0.003^{+0.009}_{-0.009}$ **	$0.003^{+0.007}_{-0.007}$ **	$0.99^{+0.01}_{-0.01}$	$0.037^{+0.003}_{-0.003}$
p	0.8 km	0.12	$0.00^{+0.02}_{-0.02}$ *	$0.01^{+0.01}_{-0.01}$ **	$-0.01^{+0.02}_{-0.02}$	$0.04^{+0.01}_{-0.01}$ **	$0.96^{+0.01}_{-0.01}$	$0.08^{+0.01}_{-0.01}$
w	0.3 km	0.04	$-0.02^{+0.02}_{-0.02}$ ***	$-0.01^{+0.01}_{-0.01}$ ***	$0.03^{+0.03}_{-0.02}$ ***	$-0.01^{+0.02}_{-0.02}$**	$1.05^{+0.01}_{-0.01}$	$0.10^{+0.01}_{-0.01}$
y	0.35 km	0.04	$0.00^{+0.01}_{-0.01}$ *	$-0.006^{+0.006}_{-0.006}$ ***	$0.01^{+0.01}_{-0.01}$ **	$0.015^{+0.008}_{-0.008}$	$0.980^{+0.006}_{-0.006}$	$0.045^{+0.004}_{-0.003}$
b	0 km	0.11	$-0.010^{+0.006}_{-0.006}$	$-0.005^{+0.004}_{-0.004}$	$0.001^{+0.006}_{-0.006}$ *	$0.006^{+0.005}_{-0.005}$	$0.996^{+0.004}_{-0.004}$	$0.027^{+0.002}_{-0.002}$

*, **, and *** indicate measurements consistent with zero within 1σ, 2σ, or 3σ uncertainty, respectively.

References

1. Theobald, D.M. Development and applications of a comprehensive land use classification and map for the US. *PLoS ONE* **2014**, *9*, e94628.
2. Schneider, A.; Friedl, M.; Potere, D. A new map of global urban extent from MODIS data. *Environ. Res. Lett.* **2009**, *4*, 44003–44011. https://doi.org/10.1088/1748-9326/4/4/044003.
3. Nations, U. *2018 Revision of World Urbanization Prospects*; Population Division of the UN Department of Economic and Social Affairs (UN DESA): New York, NY, USA, 2018.
4. Akimoto, H. Global air quality and pollution. *Science* **2003**, *302*, 1716–1719.
5. Stone, B., Jr. Urban sprawl and air quality in large US cities. *J. Environ. Manag.* **2008**, *86*, 688–698.
6. Butt, E.; Turnock, S.; Rigby, R.; Reddington, C.; Yoshioka, M.; Johnson, J.; Regayre, L.; Pringle, K.; Mann, G.; Spracklen, D. Global and regional trends in particulate air pollution and attributable health burden over the past 50 years. *Environ. Res. Lett.* **2017**, *12*, 104017.
7. Ostro, B.; World Health Organization. *Outdoor Air Pollution: Assessing the Environmental Burden of Disease at National and Local Levels*; World Health Organization: Geneva, Switzerland, 2004.
8. Cohen, A.J.; Ross Anderson, H.; Ostro, B.; Pandey, K.D.; Krzyzanowski, M.; Künzli, N.; Gutschmidt, K.; Pope, A.; Romieu, I.; Samet, J.M.; et al. The global burden of disease due to outdoor air pollution. *J. Toxicol. Environ. Heal. Part A* **2005**, *68*, 1301–1307.
9. Gurjar, B.; Jain, A.; Sharma, A.; Agarwal, A.; Gupta, P.; Nagpure, A.S.; Lelieveld, J. Human health risks in megacities due to air pollution. *Atmos. Environ.* **2010**, *44*, 4606–4613.
10. Lim, S.S.; Vos, T.; Flaxman, A.D.; Danaei, G.; Shibuya, K.; Adair-Rohani, H.; AlMazroa, M.A.; Amann, M.; Anderson, H.R.; Andrews, K.G.; et al. A comparative risk assessment of burden of disease and injury attributable to 67 risk factors and risk factor clusters in 21 regions, 1990–2010: A systematic analysis for the Global Burden of Disease Study 2010. *Lancet* **2012**, *380*, 2224–2260.
11. Cohen, A.J.; Brauer, M.; Burnett, R.; Anderson, H.R.; Frostad, J.; Estep, K.; Balakrishnan, K.; Brunekreef, B.; Dandona, L.; Dandona, R.; et al. Estimates and 25-year trends of the global burden of disease attributable to ambient air pollution: An analysis of data from the Global Burden of Diseases Study 2015. *Lancet* **2017**, *389*, 1907–1918.
12. Cameron, C. The influence of chemical exhalations on agriculture. *Gard. Chron.* **1874**, *1*, 274–275.
13. Ruston, A.G. Plant as an index of smoke pollution. *Ann. Appl. Biol.* **1921**, *7*, 390–403. https://doi.org/10.1111/j.1744-7348.1921.tb05526.x.
14. Darley, E.; Middleton, J. Problems of air pollution in plant pathology. *Annu. Rev. Phytopathol.* **1966**, *4*, 103–118.
15. Hongfa, C. Air Pollution and Its Effects on Plants in China. *J. Appl. Ecol.* **1989**, *26*, 763–773.
16. Honour, S.L.; Bell, J.N.B.; Ashenden, T.W.; Cape, J.N.; Power, S.A. Responses of herbaceous plants to urban air pollution: Effects on growth, phenology and leaf surface characteristics. *Environ. Pollut.* **2009**, *157*, 1279–1286. https://doi.org/10.1016/j.envpol.2008.11.049.
17. Rai, P.; Panda, L. Roadside plants as bio indicators of air pollution in an industrial region, Rourkela, India. *Int. J. Adv. Res. Technol.* **2015**, *4*, 14–36.
18. Rai, P.K. Biodiversity of roadside plants and their response to air pollution in an Indo-Burma hotspot region: Implications for urban ecosystem restoration. *J. Asia-Pac. Biodivers.* **2016**, *9*, 47–55.
19. Chaudhary, I.J.; Rathore, D. Suspended particulate matter deposition and its impact on urban trees. *Atmos. Pollut. Res.* **2018**, *9*, 1072–1082.
20. Ranjan, O.; Menon, J.S.; Nagendra, S.S. Assessment of air quality impacts on human health and vegetation at an industrial area. *J. Hazardous Toxic Radioact. Waste* **2016**, *20*, A4016002.
21. Karnosky, D.F.; Skelly, J.M.; Percy, K.E.; Chappelka, A.H. Perspectives regarding 50 years of research on effects of tropospheric ozone air pollution on US forests. *Environ. Pollut.* **2007**, *147*, 489–506.
22. Mills, G.; Pleijel, H.; Braun, S.; Büker, P.; Bermejo, V.; Calvo, E.; Danielsson, H.; Emberson, L.; Fernández, I.G.; Grünhage, L.; et al. New stomatal flux-based critical levels for ozone effects on vegetation. *Atmos. Environ.* **2011**, *45*, 5064–5068.

23. Fares, S.; Vargas, R.; Detto, M.; Goldstein, A.H.; Karlik, J.; Paoletti, E.; Vitale, M. Tropospheric ozone reduces carbon assimilation in trees: Estimates from analysis of continuous flux measurements. *Glob. Chang. Biol.* **2013**, *19*, 2427–2443.
24. Sicard, P.; Anav, A.; De Marco, A.; Paoletti, E. Projected global ground-level ozone impacts on vegetation under different emission and climate scenarios. *Atmos. Chem. Phys.* **2017**, *17*, 12177.
25. Mills, G.; Hayes, F.; Simpson, D.; Emberson, L.; Norris, D.; Harmens, H.; Büker, P. Evidence of widespread effects of ozone on crops and (semi-) natural vegetation in Europe (1990–2006) in relation to AOT40-and flux-based risk maps. *Glob. Chang. Biol.* **2011**, *17*, 592–613.
26. Grünhage, L.; Pleijel, H.; Mills, G.; Bender, J.; Danielsson, H.; Lehmann, Y.; Castell, J.F.; Bethenod, O. Updated stomatal flux and flux-effect models for wheat for quantifying effects of ozone on grain yield, grain mass and protein yield. *Environ. Pollut.* **2012**, *165*, 147–157.
27. Bytnerowicz, A.; Alonso, R.; Arbaugh, M. *Ozone Air Pollution in the Sierra Nevada-Distribution and Effects on Forests*; Elsevier: Amsterdam, The Netherlands, 2003.
28. Paoletti, E. Ozone impacts on forests. *CAB Rev. Perspect. Agric. Vet. Sci. Nutr. Nat. Resour.* **2007**, *2*, 13.
29. Sicard, P.; De Marco, A.; Dalstein-Richier, L.; Tagliaferro, F.; Renou, C.; Paoletti, E. An epidemiological assessment of stomatal ozone flux-based critical levels for visible ozone injury in Southern European forests. *Sci. Total Environ.* **2016**, *541*, 729–741.
30. Karlsson, P.; Pleijel, H.; Karlsson, G.P.; Medin, E.; Skärby, L. Simulations of stomatal conductance and ozone uptake to Norway spruce saplings in open-top chambers. *Environ. Pollut.* **2000**, *109*, 443–451.
31. Manning, W.J. Establishing a cause and effect relationship for ambient ozone exposure and tree growth in the forest: Progress and an experimental approach. *Environ. Pollut.* **2005**, *137*, 443–454.
32. Paoletti, E. Ozone and urban forests in Italy. *Environ. Pollut.* **2009**, *157*, 1506–1512.
33. Leung, F.; Pang, J.; Tai, A.P.; Lam, T.; Tao, D.K.; Sharps, K. Evidence of ozone-induced visible foliar injury in Hong Kong using Phaseolus vulgaris as a bioindicator. *Atmosphere* **2020**, *11*, 266.
34. Bloomer, B.J.; Stehr, J.W.; Piety, C.A.; Salawitch, R.J.; Dickerson, R.R. Observed relationships of ozone air pollution with temperature and emissions. *Geophys. Res. Lett.* **2009**, *36*, L09803.
35. Camalier, L.; Cox, W.; Dolwick, P. The effects of meteorology on ozone in urban areas and their use in assessing ozone trends. *Atmos. Environ.* **2007**, *41*, 7127–7137.
36. Korsog, P.E.; Wolff, G.T. An examination of urban ozone trends in the northeastern US (1973–1983) using a robust statistical method. *Atmos. Environment. Part B. Urban Atmos.* **1991**, *25*, 47–57.
37. Wallace, J.; Kanaroglou, P. The effect of temperature inversions on ground-level nitrogen dioxide (NO2) and fine particulate matter (PM2. 5) using temperature profiles from the Atmospheric Infrared Sounder (AIRS). *Sci. Total Environ.* **2009**, *407*, 5085–5095.
38. Janhäll, S.; Olofson, K.F.G.; Andersson, P.U.; Pettersson, J.B.; Hallquist, M. Evolution of the urban aerosol during winter temperature inversion episodes. *Atmos. Environ.* **2006**, *40*, 5355–5366.
39. Peñuelas, J.; Filella, I. Phenology feedbacks on climate change. *Science* **2009**, *324*, 887–888.
40. Chuine, I. Why does phenology drive species distribution? *Philos. Trans. R. Soc. B Biol. Sci.* **2010**, *365*, 3149–3160.
41. Hänninen, H. Boreal and temperate trees in a changing climate. In *Biometeorology*; Springer: Dordrecht, The Netherlands, 2016.
42. Fu, Y.H.; Piao, S.; Op de Beeck, M.; Cong, N.; Zhao, H.; Zhang, Y.; Menzel, A.; Janssens, I.A. Recent spring phenology shifts in western C entral E urope based on multiscale observations. *Glob. Ecol. Biogeogr.* **2014**, *23*, 1255–1263.
43. Beaubien, E.; Freeland, H. Spring phenology trends in Alberta, Canada: Links to ocean temperature. *Int. J. Biometeorol.* **2000**, *44*, 53–59.
44. Menzel, A.; Fabian, P. Growing season extended in Europe. *Nature* **1999**, *397*, 659–659.
45. Zhang, X.; Friedl, M.A.; Schaaf, C.B.; Strahler, A.H. Climate controls on vegetation phenological patterns in northern mid-and high latitudes inferred from MODIS data. *Glob. Chang. Biol.* **2004**, *10*, 1133–1145.
46. Fu, Y.H.; Piao, S.; Zhao, H.; Jeong, S.J.; Wang, X.; Vitasse, Y.; Ciais, P.; Janssens, I.A. Unexpected role of winter precipitation in determining heat requirement for spring vegetation green-up at northern middle and high latitudes. *Glob. Chang. Biol.* **2014**, *20*, 3743–3755.
47. Liu, Q.; Fu, Y.H.; Zeng, Z.; Huang, M.; Li, X.; Piao, S. Temperature, precipitation, and insolation effects on autumn vegetation phenology in temperate China. *Glob. Chang. Biol.* **2016**, *22*, 644–655.
48. Pavón, N.P.; Briones, O. Phenological patterns of nine perennial plants in an intertropical semi-arid Mexican scrub. *J. Arid Environ.* **2001**, *49*, 265–277.
49. Han, G.; Xu, J. Land surface phenology and land surface temperature changes along an urban–rural gradient in Yangtze River Delta, China. *Environ. Manag.* **2013**, *52*, 234–249.
50. Jochner, S.; Menzel, A. Urban phenological studies—Past, present, future. *Environ. Pollut.* **2015**, *203*, 250–261. https://doi.org/10.1016/j.envpol.2015.01.003.
51. Gibbons, P.; Freudenberger, D. An overview of methods used to assess vegetation condition at the scale of the site. *Ecol. Manag. Restor.* **2006**, *7*, S10–S17.
52. Pu, R.; Kelly, M.; Anderson, G.L.; Gong, P. Using CASI hyperspectral imagery to detect mortality and vegetation stress associated with a new hardwood forest disease. *Photogramm. Eng. Remote Sens.* **2008**, *74*, 65–75.
53. Kopačková, V.; Mišurec, J.; Lhotáková, Z.; Oulehle, F.; Albrechtová, J. Using multi-date high spectral resolution data to assess the physiological status of macroscopically undamaged foliage on a regional scale. *Int. J. Appl. Earth Obs. Geoinf.* **2014**, *27*, 169–186.

54. Lowe, A.; Harrison, N.; French, A.P. Hyperspectral image analysis techniques for the detection and classification of the early onset of plant disease and stress. *Plant Methods* **2017**, *13*, 80.
55. Geladi, P.; Grahn, H.; Burger, J. Multivariate images, hyperspectral imaging: Background and equipment. In *Techniques and Applications of Hyperspectral Image Analysis*; John Wiley & Sons: West Sussex, UK, 2007; pp. 1–15.
56. Zhang, M.; Qin, Z.; Liu, X.; Ustin, S.L. Detection of stress in tomatoes induced by late blight disease in California, USA, using hyperspectral remote sensing. *Int. J. Appl. Earth Obs. Geoinf.* **2003**, *4*, 295–310.
57. Bauriegel, E.; Giebel, A.; Geyer, M.; Schmidt, U.; Herppich, W. Early detection of Fusarium infection in wheat using hyper-spectral imaging. *Comput. Electron. Agric.* **2011**, *75*, 304–312.
58. Behmann, J.; Bohnenkamp, D.; Paulus, S.; Mahlein, A.K. Spatial referencing of hyperspectral images for tracing of plant disease symptoms. *J. Imaging* **2018**, *4*, 143.
59. Chaerle, L.; Van Der Straeten, D. Imaging techniques and the early detection of plant stress. *Trends Plant Sci.* **2000**, *5*, 495–501.
60. Tilling, A.K.; O'Leary, G.J.; Ferwerda, J.G.; Jones, S.D.; Fitzgerald, G.J.; Rodriguez, D.; Belford, R. Remote sensing of nitrogen and water stress in wheat. *Field Crop. Res.* **2007**, *104*, 77–85.
61. Behmann, J.; Steinrücken, J.; Plümer, L. Detection of early plant stress responses in hyperspectral images. *ISPRS J. Photogramm. Remote Sens.* **2014**, *93*, 98–111.
62. Carlson, T.N.; Ripley, D.A. On the relation between NDVI, fractional vegetation cover, and leaf area index. *Remote Sens. Environ.* **1997**, *62*, 241–252.
63. Gamon, J.; Penuelas, J.; Field, C. A narrow-waveband spectral index that tracks diurnal changes in photosynthetic efficiency. *Remote Sens. Environ.* **1992**, *41*, 35–44.
64. Žibret, G.; Kopačková, V. Comparison of two methods for indirect measurement of atmospheric dust deposition: Street-dust composition and vegetation-health status derived from hyperspectral image data. *Ambio* **2019**, *48*, 423–435.
65. Shanmugapriya, P.; Rathika, S.; Ramesh, T.; Janaki, P. Applications of remote sensing in agriculture-A Review. *Int. J. Curr. Microbiol. Appl. Sci.* **2019**, *8*, 2270–2283.
66. White, M.A.; de Beurs, K.M.; Didan, K.; Inouye, D.W.; Richardson, A.D.; Jensen, O.P.; O'KEEFE, J.; Zhang, G.; Nemani, R.R.; van Leeuwen, W.J.; et al. Intercomparison, interpretation, and assessment of spring phenology in North America estimated from remote sensing for 1982–2006. *Glob. Chang. Biol.* **2009**, *15*, 2335–2359.
67. Wehr, R.; Commane, R.; Munger, J.W.; McManus, J.B.; Nelson, D.D.; Zahniser, M.S.; Saleska, S.R.; Wofsy, S.C. Dynamics of canopy stomatal conductance, transpiration, and evaporation in a temperate deciduous forest, validated by carbonyl sulfide uptake. *Biogeosciences* **2017**, *14*, 389–401.
68. Chow, W.T.; Salamanca, F.; Georgescu, M.; Mahalov, A.; Milne, J.M.; Ruddell, B.L. A multi-method and multi-scale approach for estimating city-wide anthropogenic heat fluxes. *Atmos. Environ.* **2014**, *99*, 64–76.
69. Nasahara, K.N.; Nagai, S. Development of an in situ observation network for terrestrial ecological remote sensing: The Phenological Eyes Network (PEN). *Ecol. Res.* **2015**, *30*, 211–223.
70. Richardson, A.D.; Hufkens, K.; Milliman, T.; Aubrecht, D.M.; Chen, M.; Gray, J.M.; Johnston, M.R.; Keenan, T.F.; Klosterman, S.T.; Kosmala, M.; et al. Tracking vegetation phenology across diverse North American biomes using PhenoCam imagery. *Sci. Data* **2018**, *5*, 1–24.
71. Dobler, G.; Bianco, F.B.; Sharma, M.S.; Karpf, A.; Baur, J.; Ghandehari, M.; Wurtele, J.; Koonin, S.E. The Urban Observatory: A Multi-Modal Imaging Platform for the Study of Dynamics in Complex Urban Systems. *Remote Sens.* **2021**, *13*, 1426.
72. Dobler, G.; Ghandehari, M.; Koonin, S.E.; Nazari, R.; Patrinos, A.; Sharma, M.S.; Tafvizi, A.; Vo, H.T.; Wurtele, J.S. Dynamics of the urban lightscape. *Inf. Syst.* **2015**, *54*, 115–126.
73. Dobler, G.; Ghandehari, M.; Koonin, S.E.; Sharma, M.S. A hyperspectral survey of New York City lighting technology. *Sensors* **2016**, *16*, 2047.
74. Qamar, F.; Dobler, G. Pixel-Wise Classification of High-Resolution Ground-Based Urban Hyperspectral Images with Convolutional Neural Networks. *Remote Sens.* **2020**, *12*, 2540.
75. Taoufiq, S.; Nagy, B.; Benedek, C. Hierarchynet: Hierarchical CNN-based urban building classification. *Remote Sens.* **2020**, *12*, 3794.
76. Wu, H.; Li, D.; Wang, Y.; Li, X.; Kong, F.; Wang, Q. Hyperspectral Image Classification Based on Two-Branch Spectral–Spatial-Feature Attention Network. *Remote Sens.* **2021**, *13*, 4262.
77. Lassiter, A.; Darbari, M. Assessing alternative methods for unsupervised segmentation of urban vegetation in very high-resolution multispectral aerial imagery. *PLoS ONE* **2020**, *15*, e0230856.
78. Sabater, N.; Vicent, J.; Alonso, L.; Cogliati, S.; Verrelst, J.; Moreno, J. Impact of atmospheric inversion effects on solar-induced chlorophyll fluorescence: Exploitation of the apparent reflectance as a quality indicator. *Remote Sens.* **2017**, *9*, 622.
79. Campbell, P.E.; Middleton, E.; Corp, L.; Kim, M. Contribution of chlorophyll fluorescence to the apparent vegetation reflectance. *Sci. Total Environ.* **2008**, *404*, 433–439.
80. Gao, B.C.; Heidebrecht, K.B.; Goetz, A.F. Derivation of scaled surface reflectances from AVIRIS data. *Remote Sens. Environ.* **1993**, *44*, 165–178.
81. Staenz, K.; Secker, J.; Gao, B.C.; Davis, C.; Nadeau, C. Radiative transfer codes applied to hyperspectral data for the retrieval of surface reflectance. *ISPRS J. Photogramm. Remote Sens.* **2002**, *57*, 194–203.

82. Qamar, F.; Gómez-Fonseca, A.S.; Dobler, G. The Effects of Atmospheric Modeling Covariance on Ground-Based Hyperspectral Measurements of Surface Reflectance. In Proceedings of the 2021 11th Workshop on Hyperspectral Imaging and Signal Processing: Evolution in Remote Sensing (WHISPERS), Amsterdam, The Netherlands, 24–26 March 2021; pp. 1–5. https://doi.org/10.1109/WHISPERS52202.2021.9483972.
83. Damm, A.; Guanter, L.; Verhoef, W.; Schläpfer, D.; Garbari, S.; Schaepman, M.E. Impact of varying irradiance on vegetation indices and chlorophyll fluorescence derived from spectroscopy data. *Remote Sens. Environ.* **2015**, *156*, 202–215.
84. Zhang, Z.; Zhang, Y.; Zhang, Q.; Chen, J.M.; Porcar-Castell, A.; Guanter, L.; Wu, Y.; Zhang, X.; Wang, H.; Ding, D.; et al. Assessing bi-directional effects on the diurnal cycle of measured solar-induced chlorophyll fluorescence in crop canopies. *Agric. For. Meteorol.* **2020**, *295*, 108147.
85. Cho, H.J.; Kirui, P.; Natarajan, H. Test of multi-spectral vegetation index for floating and canopy-forming submerged vegetation. *Int. J. Environ. Res. Public Health* **2008**, *5*, 477–483.
86. Fedotov, Y.; Bullo, O.; Belov, M.; Gorodnichev, V. Experimental research of reliability of plant stress state detection by laser-induced fluorescence method. *Int. J. Opt.* **2016**, *2016*.
87. Williams, R.; Kilaru, V.; Snyder, E.; Kaufman, A.; Dye, T.; Rutter, A.; Russell, A.; Hafner, H. *Air Sensor Guidebook*; US Environmental Protection Agency: Washington, DC, USA, 2014.
88. Maag, B.; Zhou, Z.; Thiele, L. A survey on sensor calibration in air pollution monitoring deployments. *IEEE Internet Things J.* **2018**, *5*, 4857–4870.
89. Maag, B. Air Quality Sensor Calibration and Its Peculiarities. Ph.D. Thesis, ETH Zurich, Zurich, Switzerland, 2019.
90. Concas, F.; Mineraud, J.; Lagerspetz, E.; Varjonen, S.; Liu, X.; Puolamäki, K.; Nurmi, P.; Tarkoma, S. Low-cost outdoor air quality monitoring and sensor calibration: A survey and critical analysis. *ACM Trans. Sens. Netw. (TOSN)* **2021**, *17*, 1–44.
91. Stathopoulou, E.; Mihalakakou, G.; Santamouris, M.; Bagiorgas, H. On the impact of temperature on tropospheric ozone concentration levels in urban environments. *J. Earth Syst. Sci.* **2008**, *117*, 227–236.
92. Zhu, J.; Chen, L.; Liao, H.; Dang, R. Correlations between PM2. 5 and ozone over China and associated underlying reasons. *Atmosphere* **2019**, *10*, 352.
93. Carter, G.A. Responses of leaf spectral reflectance to plant stress. *Am. J. Bot.* **1993**, *80*, 239–243.
94. Mahlein, A.K. Plant disease detection by imaging sensors—Parallels and specific demands for precision agriculture and plant phenotyping. *Plant Dis.* **2016**, *100*, 241–251.
95. Vogelmann, T.C. Plant tissue optics. *Annu. Rev. Plant Biol.* **1993**, *44*, 231–251.
96. Gitelson, A.A.; Zur, Y.; Chivkunova, O.B.; Merzlyak, M.N. Assessing carotenoid content in plant leaves with reflectance spectroscopy. *Photochem. Photobiol.* **2002**, *75*, 272–281.
97. Zarco-Tejada, P.J.; Hornero, A.; Beck, P.; Kattenborn, T.; Kempeneers, P.; Hernández-Clemente, R. Chlorophyll content estimation in an open-canopy conifer forest with Sentinel-2A and hyperspectral imagery in the context of forest decline. *Remote Sens. Environ.* **2019**, *223*, 320–335.
98. Slaton, M.R.; Raymond Hunt Jr, E.; Smith, W.K. Estimating near-infrared leaf reflectance from leaf structural characteristics. *Am. J. Bot.* **2001**, *88*, 278–284.
99. Yang, B.; He, Y.; Chen, W. A simple method for estimation of leaf dry matter content in fresh leaves using leaf scattering albedo. *Glob. Ecol. Conserv.* **2020**, *23*, e01201.
100. Daughtry, C.S.; Walthall, C.; Kim, M.; De Colstoun, E.B.; McMurtrey, J., III. Estimating corn leaf chlorophyll concentration from leaf and canopy reflectance. *Remote Sens. Environ.* **2000**, *74*, 229–239.
101. Pavlovic, D.; Nikolic, B.; Djurovic, S.; Waisi, H.; Andjelkovic, A.; Marisavljevic, D. Chlorophyll as a measure of plant health: Agroecological aspects. *Pestic. I Fitomedicina* **2015**, *29*. https://doi.org/10.2298/PIF1401021P.
102. Adams, M.L.; Philpot, W.D.; Norvell, W.A. Yellowness index: An application of spectral second derivatives to estimate chlorosis of leaves in stressed vegetation. *Int. J. Remote Sens.* **1999**, *20*, 3663–3675.
103. Biswal, B. Carotenoid catabolism during leaf senescence and its control by light. *J. Photochem. Photobiol. B: Biol.* **1995**, *30*, 3–13.
104. Windt, C.W.; Nabel, M.; Kochs, J.; Jahnke, S.; Schurr, U. A Mobile NMR Sensor and Relaxometric Method to Non-destructively Monitor Water and Dry Matter Content in Plants. *Front. Plant Sci.* **2021**, *12*, 18.
105. Liu, L.; Wang, J.; Huang, W.; Zhao, C.; Zhang, B.; Tong, Q. Estimating winter wheat plant water content using red edge parameters. *Int. J. Remote Sens.* **2004**, *25*, 3331–3342.
106. Wocher, M.; Berger, K.; Danner, M.; Mauser, W.; Hank, T. Physically-based retrieval of canopy equivalent water thickness using hyperspectral data. *Remote Sens.* **2018**, *10*, 1924.
107. Kakani, V.G.; Reddy, K.R.; Zhao, D.; Gao, W. Senescence and hyperspectral reflectance of cotton leaves exposed to ultraviolet-B radiation and carbon dioxide. *Physiol. Plant.* **2004**, *121*, 250–257.
108. Tol, C.; Verhoef, W.; Timmermans, J.; Verhoef, A.; Su, Z. An integrated model of soil-canopy spectral radiances, photosynthesis, fluorescence, temperature and energy balance. *Biogeosciences* **2009**, *6*, 3109–3129.
109. Yang, P.; Prikaziuk, E.; Verhoef, W.; van der Tol, C. SCOPE 2.0: A model to simulate vegetated land surface fluxes and satellite signals. *Geosci. Model Dev.* **2021**, *14*, 4697–4712.
110. Porcar-Castell, A.; Tyystjärvi, E.; Atherton, J.; Van der Tol, C.; Flexas, J.; Pfündel, E.E.; Moreno, J.; Frankenberg, C.; Berry, J.A. Linking chlorophyll a fluorescence to photosynthesis for remote sensing applications: Mechanisms and challenges. *J. Exp. Bot.* **2014**, *65*, 4065–4095.

111. Sun, Y.; Frankenberg, C.; Wood, J.D.; Schimel, D.; Jung, M.; Guanter, L.; Drewry, D.; Verma, M.; Porcar-Castell, A.; Griffis, T.J.; et al. OCO-2 advances photosynthesis observation from space via solar-induced chlorophyll fluorescence. *Science* **2017**, *358*, eaam5747.
112. Zarco-Tejada, P.J.; Catalina, A.; González, M.; Martín, P. Relationships between net photosynthesis and steady-state chlorophyll fluorescence retrieved from airborne hyperspectral imagery. *Remote Sens. Environ.* **2013**, *136*, 247–258.
113. Damm, A.; Guanter, L.; Paul-Limoges, E.; Van der Tol, C.; Hueni, A.; Buchmann, N.; Eugster, W.; Ammann, C.; Schaepman, M.E. Far-red sun-induced chlorophyll fluorescence shows ecosystem-specific relationships to gross primary production: An assessment based on observational and modeling approaches. *Remote Sens. Environ.* **2015**, *166*, 91–105.
114. Baker, N.R. Chlorophyll fluorescence: A probe of photosynthesis in vivo. *Annu. Rev. Plant Biol.* **2008**, *59*, 89–113.
115. Ač, A.; Malenovskỳ, Z.; Olejníčková, J.; Galle, A.; Rascher, U.; Mohammed, G. Meta-analysis assessing potential of steady-state chlorophyll fluorescence for remote sensing detection of plant water, temperature and nitrogen stress. *Remote Sens. Environ.* **2015**, *168*, 420–436.
116. Plascyk, J.A. The MK II Fraunhofer line discriminator (FLD-II) for airborne and orbital remote sensing of solar-stimulated luminescence. *Opt. Eng.* **1975**, *14*, 144339.
117. Plascyk, J.A.; Gabriel, F.C. The Fraunhofer line discriminator MKII-an airborne instrument for precise and standardized ecological luminescence measurement. *IEEE Trans. Instrum. Meas.* **1975**, *24*, 306–313.
118. Maier, S.W.; Günther, K.P.; Stellmes, M. Sun-induced fluorescence: A new tool for precision farming. *Digit. Imaging Spectr. Tech. Appl. Precis. Agric. Crop Physiol.* **2004**, *66*, 207–222.
119. GomezChova, L.; AlonsoChorda, L.; Amoros Lopez, J.; Vila Frances, J.; del ValleTascon, S.; Calpe, J.; Moreno, J. Solar induced fluorescence measurements using a field spectroradiometer. *AIP Conf. Proc.* **2006**, *852*, 274–281, https://doi.org/10.1063/1.2349354.
120. Alonso, L.; Gomez-Chova, L.; Vila-Frances, J.; Amoros-Lopez, J.; Guanter, L.; Calpe, J.; Moreno, J. Improved Fraunhofer Line Discrimination method for vegetation fluorescence quantification. *IEEE Geosci. Remote Sens. Lett.* **2008**, *5*, 620–624.
121. Zhao, F.; Guo, Y.; Verhoef, W.; Gu, X.; Liu, L.; Yang, G. A method to reconstruct the solar-induced canopy fluorescence spectrum from hyperspectral measurements. *Remote Sens.* **2014**, *6*, 10171–10192.
122. Verhoef, W.; Van Der Tol, C.; Middleton, E.M. Hyperspectral radiative transfer modeling to explore the combined retrieval of biophysical parameters and canopy fluorescence from FLEX–Sentinel-3 tandem mission multi-sensor data. *Remote Sens. Environ.* **2018**, *204*, 942–963.
123. Zarco-Tejada, P.J.; Miller, J.R.; Mohammed, G.H.; Noland, T.L. Chlorophyll fluorescence effects on vegetation apparent reflectance: I. Leaf-level measurements and model simulation. *Remote Sens. Environ.* **2000**, *74*, 582–595.
124. Zarco-Tejada, P.J.; Miller, J.R.; Mohammed, G.H.; Noland, T.L.; Sampson, P.H. Chlorophyll fluorescence effects on vegetation apparent reflectance: II. Laboratory and airborne canopy-level measurements with hyperspectral data. *Remote Sens. Environ.* **2000**, *74*, 596–608.
125. Zarco-Tejada, P.J.; Pushnik, J.; Dobrowski, S.; Ustin, S. Steady-state chlorophyll a fluorescence detection from canopy derivative reflectance and double-peak red-edge effects. *Remote Sens. Environ.* **2003**, *84*, 283–294.
126. Dobrowski, S.; Pushnik, J.; Zarco-Tejada, P.J.; Ustin, S.L. Simple reflectance indices track heat and water stress-induced changes in steady-state chlorophyll fluorescence at the canopy scale. *Remote Sens. Environ.* **2005**, *97*, 403–414.
127. Xing, X.G.; Zhao, D.Z.; Liu, Y.G.; Yang, J.H.; Xiu, P.; Wang, L. An overview of remote sensing of chlorophyll fluorescence. *Ocean Sci. J.* **2007**, *42*, 49–59.
128. Badgley, G.; Field, C.B.; Berry, J.A. Canopy near-infrared reflectance and terrestrial photosynthesis. *Sci. Adv.* **2017**, *3*, e1602244.
129. Zeng, Y.; Hao, D.; Badgley, G.; Damm, A.; Rascher, U.; Ryu, Y.; Johnson, J.; Krieger, V.; Wu, S.; Qiu, H.; et al. Estimating near-infrared reflectance of vegetation from hyperspectral data. *Remote Sens. Environ.* **2021**, *267*, 112723.
130. Roujean, J.L.; Breon, F.M. Estimating PAR absorbed by vegetation from bidirectional reflectance measurements. *Remote Sens. Environ.* **1995**, *51*, 375–384.
131. Agarwal, A.; El-Ghazawi, T.; El-Askary, H.; Le-Moigne, J. Efficient hierarchical-PCA dimension reduction for hyperspectral imagery. In Proceedings of the 2007 IEEE International Symposium on Signal Processing and Information Technology, Giza, Egypt, 15–18 December 2007; pp. 353–356.
132. ZhengYang, Z.; XinMing, M.; GuoShun, L.; FangFang, J.; HongBo, Q.; YingWu, Z.; Shizhao, L.; WenFeng, S. A study on hyperspectral estimating models of tobacco leaf area index. *Afr. J. Agric. Res.* **2011**, *6*, 289–295.
133. Foreman-Mackey, D.; Hogg, D.W.; Lang, D.; Goodman, J. emcee: The MCMC Hammer. *Publ. Astron. Soc. Pac.* **2013**, *125*, 306, https://doi.org/10.1086/670067.
134. Sweeney, A.; West, R.; O'connor, C. Parameters Affecting The Albedo Effect in Concrete. *Dep. Civil Struct. Environ. Eng. Trinity Coll. Dublin* **2011**, *2*, 1–8.
135. Qin, Y.; Zhao, Y.; Chen, X.; Wang, L.; Li, F.; Bao, T. Moist curing increases the solar reflectance of concrete. *Constr. Build. Mater.* **2019**, *215*, 114–118.
136. Pacifico, F.; Harrison, S.; Jones, C.; Sitch, S. Isoprene emissions and climate. *Atmos. Environ.* **2009**, *43*, 6121–6135.
137. Lee, B.S.; Wang, J.L. Concentration variation of isoprene and its implications for peak ozone concentration. *Atmos. Environ.* **2006**, *40*, 5486–5495.
138. Sharkey, T.D.; Wiberley, A.E.; Donohue, A.R. Isoprene emission from plants: Why and how. *Ann. Bot.* **2008**, *101*, 5–18.
139. Betts, A.K.; Desjardins, R.; Worth, D.; Beckage, B. Climate coupling between temperature, humidity, precipitation, and cloud cover over the Canadian Prairies. *J. Geophys. Res. Atmos.* **2014**, *119*, 13,305–13,326.

140. Forster, P.; Ramaswamy, V.; Artaxo, P.; Berntsen, T.; Betts, R.; Fahey, D.W.; Haywood, J.; Lean, J.; Lowe, D.C.; Myhre, G.; et al. Changes in atmospheric constituents and in radiative forcing. Chapter 2. In *Climate Change 2007. The Physical Science Basis*; Cambridge University Press: Cambridge, UK, 2007; pp. 137–152.
141. McGrath, J.; Spargo, J.; Penn, C., Soil Fertility and Plant Nutrition. In *Plant Health*; Elsevier: Amsterdam, The Netherlands, 2014; pp. 166–184. https://doi.org/10.1016/B978-0-444-52512-3.00249-7.
142. Hogan, D.M.; Walbridge, M.R. Urbanization and nutrient retention in freshwater riparian wetlands. *Ecol. Appl.* **2007**, *17*, 1142–1155.
143. Lichtenthaler, H.K.; Ač, A.; Marek, M.V.; Kalina, J.; Urban, O. Differences in pigment composition, photosynthetic rates and chlorophyll fluorescence images of sun and shade leaves of four tree species. *Plant Physiol. Biochem.* **2007**, *45*, 577–588.
144. Rouse, J.W.; Haas, R.H.; Schell, J.A.; Deering, D.W.; Harlan, J.C. *Monitoring the Vernal Advancement and Retrogradation (Green Wave Effect) of Natural Vegetation*; NASA/GSFC Type III Final Rep. Greenbelt MD; NASA Technical Reports Server (NTRS): Washington, DC, USA; 1974; Volume 371.
145. Galvão, L.S.; Ícaro Vitorello.; Filho, R.A. Effects of Band Positioning and Bandwidth on NDVI Measurements of Tropical Savannas. *Remote Sens. Environ.* **1999**, *67*, 181–193. https://doi.org/10.1016/S0034-4257(98)00085-6.